

Particle in Cell Simulation of Low Temperature Laboratory Plasmas

K. Matyash^{*1}, R. Schneider¹, F. Taccogna², A. Hatayama³, S. Longo², M. Capitelli², D. Tskhakaya⁴, and F. X. Bronold⁵

¹ Max-Planck-Institut für Plasmaphysik, EURATOM Association, Wendelsteinstrasse 1, D-17491, Greifswald, Germany

² Dipartimento di Chimica, Università degli Studi di Bari and Istituto di Metodologie Inorganiche e di Plasmi - CNR, Sect. Bari, via Orabona 4, Bari, 70126, Italy

³ Department of Applied Physics and Physico-Informatics, Faculty of Science and Technology, Keio University, 3-14-1 Hiyoshi, Kouhoku-ku, Yokohama 223-8522, Japan

⁴ Association Euratom-ÖAW, Institute of Theoretical Physics, A-6020, Innsbruck, Austria

⁵ Institut für Physik, Ernst-Moritz-Arndt-Universität Greifswald, D-17489, Greifswald, Germany

Received 18 October 2007, accepted 5 November 2007

Published online 14 December 2007

Key words Particle-in-Cell, RF discharges, dusty plasmas, negative ion sources.

PACS 52.65.Pp; 52.65.Rr; 52.80.Pi, 52.27.Lw, 52.75.Di

Several applications of PIC simulations for understanding basic physics phenomena in low-temperature plasmas are presented: capacitive radiofrequency discharges in Oxygen, dusty plasmas and negative ion sources for heating of fusion plasmas. The analysis of these systems based on their microscopic properties as accessible with PIC gives improved insight into their complex behavior. These studies are results of joint efforts over about one decade of research groups from Greifswald University, Germany; Bari University, Italy; Keio University, Japan and Innsbruck University, Austria.

© 2007 WILEY-VCH Verlag GmbH & Co. KGaA, Weinheim

1 Introduction

This is the second part of a series of three papers about Particle in Cell (PIC) simulations of low temperature plasmas. In the first paper, the basic principles of PIC were discussed. In this paper, we want to present several applications demonstrating how PIC simulations can help to understand basic physics phenomena in low-temperature plasmas. These are results of joint efforts over about one decade of research groups from Greifswald University, Germany; Bari University, Italy; Keio University, Japan and Innsbruck University, Austria.

The first example discusses capacitively coupled radio-frequency discharge. Capacitive RF discharges are widely used both in laboratory research for production of low-temperature plasmas, and in industry, where they are commonly applied for surface etching and various types of surface modification technologies [1-3]. Despite wide application of capacitive RF discharges, a complete quantitative description of such systems is still missing, in particular, with respect to characteristics of energetic particles fluxes, discharge profiles and operation regimes. This is not too surprising, because in such discharges the physics of non-equilibrium non-stationary plasmas is combined with the complexity of reactive plasma processes, including surface interaction, which makes the modeling of such systems quite challenging. In chapter 2 of this work we present the results of particle simulations of capacitive RF discharge in Oxygen with a recently developed PIC MCC code [4]. Specific emphasis was put on accurate resolution of charged particles distribution functions and their fluxes to the electrode and we concentrate on the discussion of sheath properties. The sheath determines fluxes and distribution functions of the charged particles at the electrode surface. The recently discovered phenomenon of a double emissive layer in front of the

^{*} Corresponding author: e-mail: konstantin.matyash@ipp.mpg.de
Phone: +49 (0)3834 864737, Fax: +49 (0)3834 882409

powered electrode [5] is also studied. The simulation offers here a plausible explanation and allows it to verify against the experimental measurements.

The next PIC MCC model application discussed in this paper is the simulation of dusty or complex plasmas. These plasmas in addition to electrons, ions and neutrals contain also microscopic particles of nanometer – micrometer sizes. In capacitive RF discharge the gravitational force acting on the particles can be equilibrated by the electrostatic force due to a strong repulsive electric field in the RF sheath. In this case particles are trapped in the discharge and form a cloud levitating above the lower electrode. The dust particles interact with each other through the repulsive Coulomb potential, screened by the plasma electrons and ions. In the case of strong electrostatic coupling, i.e. when the energy of the interparticle interaction is large compared to the particle thermal energy, particles self-assemble into ordered structures, known as Coulomb (plasma) crystals.

We present the results of the 2D and 3D PIC MCC simulations of dusty plasmas. The simulation features the full-scale self-consistent kinetic model of the capacitive discharge as background plasma. In the first part of chapter 3 we investigate formation of the ordered structures and the influence of the dust on the parameters of the discharge plasma. Here, dust particles are introduced in the model as additional charged species with fixed charge. In order to study the charging of the dust particle self-consistently, we have developed a 3-dimensional Particle-Particle Particle-Mesh (P^3M) model. In the model, the long-range interaction of the dust grains with charged particles of the background plasma is treated according to the PIC formalism. If particles are closer to the dust grain than a Debye length, their interaction force is computed according to a direct particle-particle MD scheme using the exact Coulomb potential. This approach allows to follow the plasma particle trajectories in the close vicinity of the dust grain and by this to include finite-size effects for dust grains. Thus, the dust grain charging due to collection of plasma electrons and ions is resolved in a self-consistent manner. In the second part of this chapter, the P^3M model is described and results of 3-dimensional simulation of the charging process of micrometer size dust grains confined in a capacitive RF discharge are presented.

Finally, we present results on the simulation of negative neutral beam injection sources for fusion. These sources are also characterized by a complicated low temperature plasma chemistry and need also kinetic models. Neutral beam injection (NBI) heating has been a reliable and powerful method to heat and drive the current of fusion plasma. At energies above 100 keV/nucleon, the neutralization efficiency for positive ions decreases drastically while staying at around 60% for negative ions. Therefore, a negative-ion-based NBI system is inevitable for a large-scaled and current-driven experimental fusion machine such as ITER, where an injection energy of 1 MeV is needed [6].

2 PIC simulation of capacitive RF discharge in Oxygen

2.1 Introduction

Capacitively coupled RF discharges consists in the simplest case of two parallel electrodes, placed in a vacuum vessel. The electrodes are powered with voltage from a RF power source. The working gas, fed into a system, gets ionized by electrons, accelerated in the RF electric field, producing the weakly-ionized plasma with an ionization degree of about 10^{-6} – 10^{-4} . The typical distance between the electrodes is of order 1-10 cm. The driving RF voltage is usually about 100-1000 V with a frequency between 1 and 100 MHz. The pressure of the working gas, depending on application of discharge, varies in the range of 1-1000 Pa. The key feature of a capacitive RF discharge, which makes it so attractive for surface processing, is the flux of energetic ions onto the substrate surface. For applications of RF discharges detailed information about plasma parameters is necessary. In case of plasma assisted surface technologies knowledge about the energy distributions of the plasma particles and their fluxes on the substrate is especially important.

During the last decade the Particle-in-Cell (PIC) simulation with Monte Carlo Collisions (MCC) has established itself as a powerful tool for modeling of capacitive RF discharges, being able to provide insight into discharge dynamics and to deliver plasma parameters which are difficult to measure directly in experiments [7-11]. Recently PIC MCC models have been successfully applied for the simulation of RF discharges with increasingly complex plasma-chemistry [12-19]. PIC simulations are useful not only for getting quantitative description for the system of interest, but also for understanding the basic physics of the discharge, helping to validate existing analytical models and to build new ones. The phenomenon of stochastic heating at low pressures, leading to bi-Maxwellian electron energy distribution functions was discovered experimentally by Godyak [20]. This was

first confirmed by PIC MCC simulations of Vahedi *et al* [10]. In [21] PIC simulation was applied to evaluate the analytical models for stochastic heating rate from [1] and [22] and finally to derive an improved formulation, which was then extended for the case of the dual frequency discharges.

Here, we present the results of particle simulations of capacitive RF discharge in Oxygen with a recently developed PIC MCC code [4]. Discharges in Oxygen are of vital importance for a large variety of etching and thin film deposition techniques [23-29]. Similar to other reactive molecular gases with internal degrees of freedom, O_2 has a quite complicated plasma-chemistry which, so far, has been analyzed primarily within global models [30-32]. The spatio-temporal variation of an O_2 discharge, however, is beyond such an approach. It can only be studied within a kinetic model [18, 19]. In fact, there is even an increasing demand for kinetic descriptions of industrial discharges because the requirements on controllability and reliability of these discharges are now so high that further advancement of this technology depends on modelling tools which reliably predict the spatial variation. Of particular interest for this system are surface modifications of polymers [33]. Therefore, specific emphasis was put on accurate resolution of charged particles distribution functions and their fluxes to the electrode and we concentrate on the discussion of sheath properties. The sheath determines fluxes and distribution functions of the charged particles at the electrode surface. The recently discovered phenomenon of a double emissive layer in front of the powered electrode [5] is also studied. The simulation offers here a plausible explanation and allows it to verify against the experimental measurements.

2.2 Simulation and Results

We simulate a parallel plate capacitive RF discharge with stainless steel circular electrodes, 9 cm in diameter and variable spacing d of 1 - 10 cm. One electrode is grounded and the second is powered from a 13.56 MHz RF voltage source. The amplitude of the driving RF voltage can be varied between 100 and 1000 V (peak to peak). Oxygen is used as a working gas, the gas pressure operation range is 1.5 – 100 Pa. The details of the experimental apparatus can be found in the [5, 33].

For the simulation, we use the PIC MCC code described in [4, 34], which uses the general algorithms described in the first paper of this series. It resolves one spatial but three velocity components (1d3v). The cross-section database for collisions in Oxygen plasma was critically assessed and corrected cross-sections for elastic scattering (O^- , O_2), recombination (O_2^+ , O^-), associative detachment (O^- , O_2) and charge exchange (O_2^+ , O_2) were implemented [4]. In total model includes 20 collisional processes (Table 1). The resulting code was successfully benchmarked against the measurements of [35].

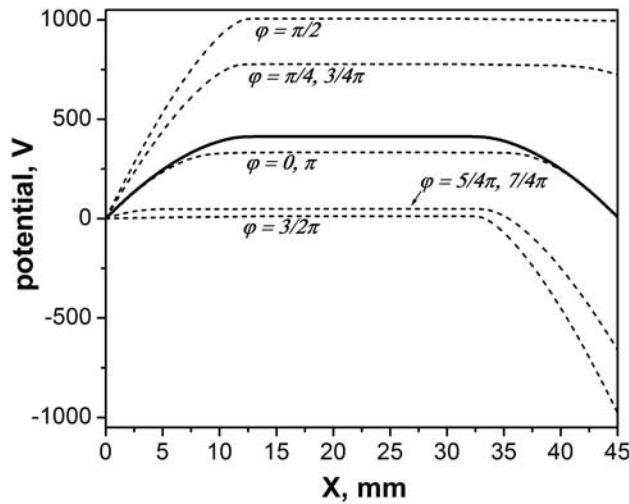
Although the simulated system is actually three-dimensional the discharge behavior is assumed to be one-dimensional along the axis. This is supported by the fact that the electrodes diameter is larger than the electrode spacing of $d = 4.5$ cm used in the simulation and that the radial dependence of the plasma parameters close to the symmetry axis can be neglected.

In the simulations, the initial electron density and temperature were chosen as $n_{e0} = 8 \cdot 10^9 \text{ cm}^{-3}$ and $T_{e0} = 10$ eV respectively. The computational domain length was $X_{\text{max}} = 172 \lambda_{D0} = 4.5$ cm. At the positions of the electrodes $X = 0$ and $X = X_{\text{max}}$ the absorbing wall boundary conditions were applied. The potential at $X = X_{\text{max}}$ was fixed at zero Volts, corresponding to the grounded electrode. At the position of the powered electrode at $X = 0$ the potential was assumed to oscillate according to the applied RF voltage: $\varphi(0, t) = U_{RF} \sin(\omega_{RF} t)$ with $\omega_{RF}/2\pi = 13.56$ MHz. Molecular Oxygen was used as a background gas. The gas temperature was $T_n = 300$ K, and pressure was varied between 5 and 60 Pa. As the neutral gas density is much higher than the densities of charged species, the neutral gas was treated as a background with fixed density and temperature. Only the dynamics of three charged particles (electrons, O_2^+ and O^- ions) was followed.

A grid size $\Delta x = \lambda_{D0}/2 = 0.013$ cm and time step $\Delta t = 0.2/\omega_{pe0} = 3.965 \cdot 10^{-11}$ s was used guaranteeing numerical stability. The number of computational particles per Debye length was chosen as $N_d = 2000$, totaling about 10^6 computational particles used in the simulation. The duration of each simulation was of the order of several thousands of RF cycles (millions of time steps) in order to ensure that the system settles to dynamic equilibrium, that is, within the statistical noise, macroscopic quantities, for instance, density and potential profiles, do not change anymore when averaged over a rf cycle.

Table 1 Collisions included in the model.

Elastic scattering		
1	$e + e \rightarrow e + e$	Coulomb scattering
2	$O^- + O^- \rightarrow O^- + O^-$	Coulomb scattering
3	$O_2^+ + O_2^+ \rightarrow O_2^+ + O_2^+$	Coulomb scattering
4	$e + O_2 \rightarrow e + O_2$	Elastic scattering
5	$O_2^+ + O_2 \rightarrow O_2^+ + O_2$	Elastic scattering
6	$O^- + O_2 \rightarrow O^- + O_2$	Elastic scattering
7	$O_2^+ + O_2 \rightarrow O_2 + O_2^+$	Charge exchange
Electron energy loss scattering		
8	$e + O_2 \rightarrow e + O_2 (\nu = 1, \dots, 4)$	Vibrational excitation
9	$e + O_2 \rightarrow e + O_2 (\text{Ryd})$	Rydberg excitation
10	$e + O_2 \rightarrow e + O(3P) + O(3P)$	Dissociation (6.4 eV)
11	$e + O_2 \rightarrow e + O(3P) + O(1D)$	Dissociation (8.6 eV)
12	$e + O_2 \rightarrow e + O_2 (a^1\Delta_g)$	Meta-stable excitation
13	$e + O_2 \rightarrow e + O_2 (b^1\Sigma_g)$	Meta-stable excitation
Electron and ion production and loss		
14	$e + O_2^+ \rightarrow O + O$	Dissociative recombination
15	$O^- + O_2^+ \rightarrow O + O_2$	Neutralization
16	$e + O_2 \rightarrow O + O^-$	Dissociative attachment
17	$O^- + O_2 \rightarrow O + O_2 + e$	Direct detachment
18	$O^- + O_2 (a^1\Delta_g) \rightarrow O_3 + e$	Associative detachment
19	$e + O_2 \rightarrow 2e + O_2^+$	Electron impact ionization
20	$e + O^- \rightarrow O + 2e$	Electron impact Detachment

**Fig. 1** Dynamics of the potential during one RF cycle (dashed lines) and the average potential during one RF cycle (solid line); $p = 5$ Pa, $U_{RF} = 1000$ V.

In fig.1 we present the axial potential profile at 8 different phases of the RF cycle as well as the potential averaged over the RF cycle for a neutral gas pressure $p = 5$ Pa and a RF voltage amplitude $U_{RF} = 1000$ V. The major potential drop takes place near the electrodes within layers of about $L_s \approx 1$ cm thickness - the RF sheaths. They are created by oscillating positive space-charge layers as discussed in [1]. The electric field in the bulk plasma is negligible in comparison with the field in the sheaths, where it is $\tilde{E}_s \approx 400$ V/cm on average. This strong electric field in the RF sheath regions is directed toward the electrodes, preventing electrons from leaving the plasma for most of the RF cycle. Electrons are able to escape to electrodes only during a short time, when the RF sheath collapses at about $\varphi = \pi/2, \varphi = 3/2\pi$.

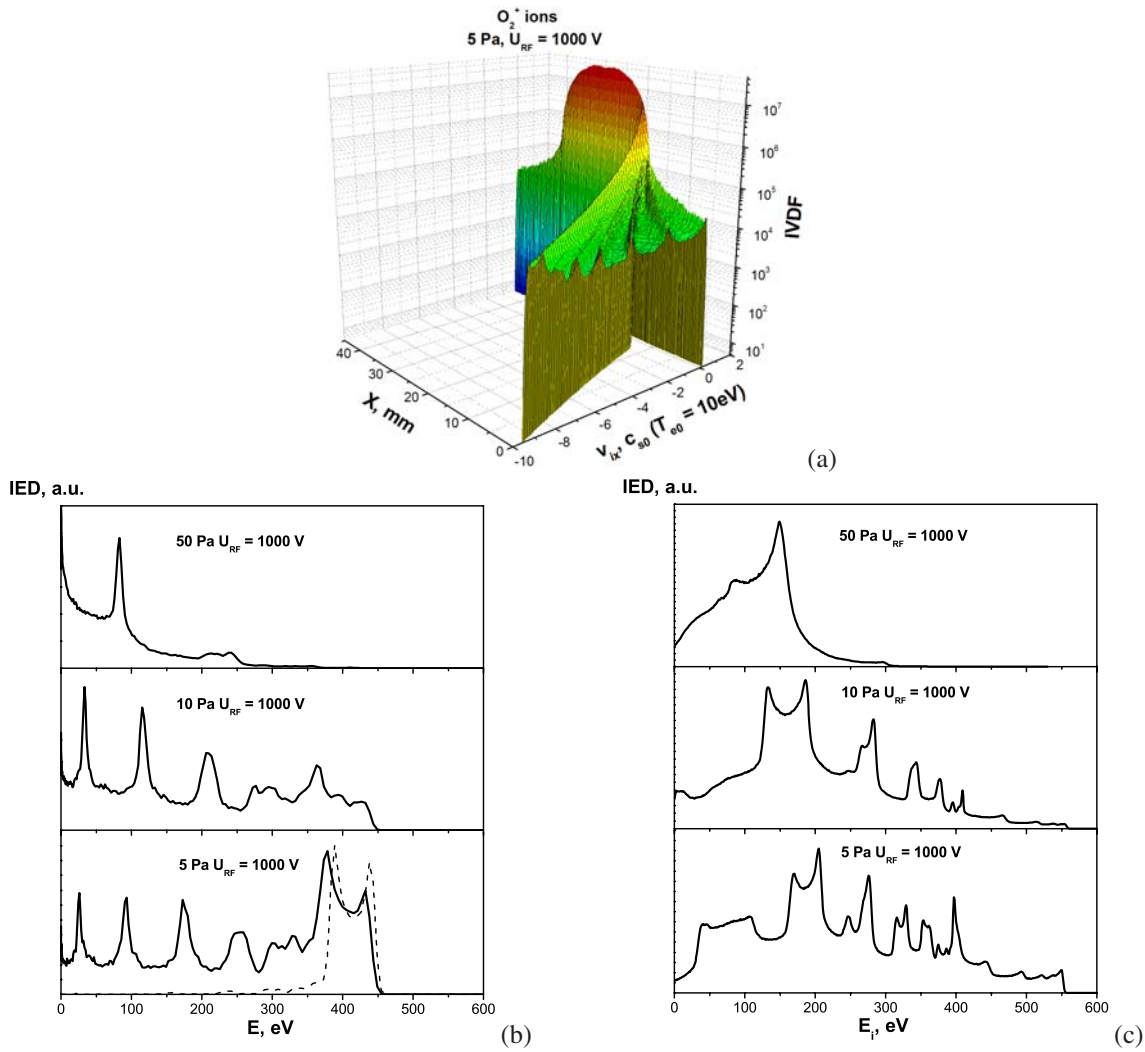
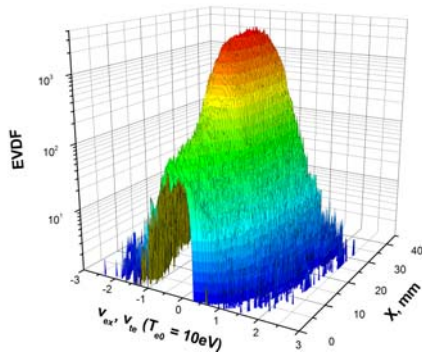


Fig. 2 O_2^+ velocity distribution (a) and O_2^+ energy distribution at the electrode position (b) averaged over RF cycle. The O_2^+ energy distribution at the electrode position measured experimentally in [40] (c). (Online colour: www.cpp-journal.org).

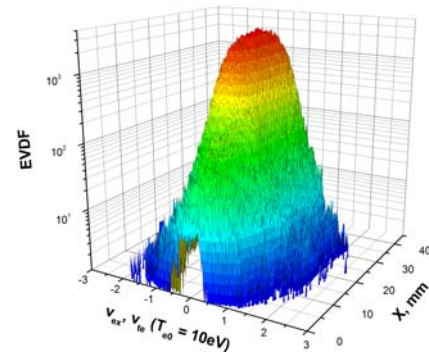
In fig.2a the profile of the distribution function of the axial velocity component for O_2^+ ions averaged over one RF cycle for $p = 5$ Pa and $U_{RF} = 1000$ V is shown. As we can see, in the bulk region the ions are cold, with an average energy close to the thermal energy of the background gas. In the sheath regions, ions are sharply accelerated in the strong electric field towards the electrodes up to the maximum energy of $E_{max} \approx 450$ eV, which is close to the average sheath potential drop. In fig.2b we plot the averaged ion energy distributions (IED) at the powered electrode position for $U_{RF} = 1000$ V and for pressures 5, 10 and 50 Pa. In the low pressure case (5 Pa) we can distinguish a characteristic saddle-like structure with two peaks in the high-energy part of the IED. This is located around the energy corresponding to the average sheath potential drop $\tilde{U}_s = 413$ V. The time that O_2^+ ions take to traverse the sheath is about $\tau_{O_2^+} \approx 2L_s / \sqrt{2e\tilde{U}_s / m_{O_2^+}} \approx 451$ ns, while the RF period is $\tau_{RF} = 2\pi / \omega_{RF} = 73.75$ ns. Therefore, it takes about 6 RF periods for O_2^+ ions to cross the sheath. The ions can only react to the average sheath potential. The saddle-like structure is populated by the ions entering the sheath in a different phase of the RF cycle. They experience a slightly different accelerating potential drop. The continuum and peaks at lower energies in the IED result from ions experiencing elastic and charge-exchange collisions with the neutral gas inside the sheath. During the charge-exchange collision a fast neutral and a slow ion with energy close to the thermal energy of the neutral gas are created. If a collision takes place inside the sheath, these ions

are experiencing only a part of the sheath acceleration. The peaks on the top of the continuum in the low energy part of IED are due to ions created by charge-exchange collisions within the sheath during the time interval when the sheath electric field collapses: $E_s \approx 0$, $\frac{dE_s}{d(\omega_{RF} t)} \approx 0$ [36-39]. Thus the number of the peaks in the IED is roughly equal to the number of RF periods it takes ions to cross the sheath.

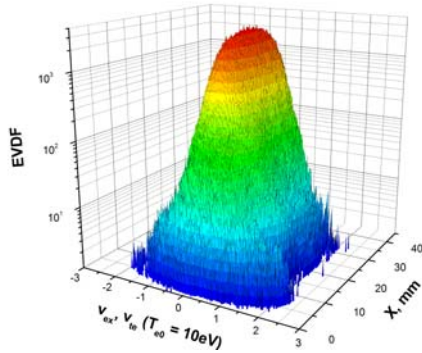
In order to distinguish the role of the ion-neutral collisions, we performed the simulation for $p = 5$ Pa and $U_{RF} = 1000$ V in which the ion-neutral elastic and the charge-exchange collisions were switched off. The resulting IED is presented in fig.2b as a dashed line. As we can see, only the saddle-like structure is pronounced, whereas the low-energy continuum is very weak, because in this case it is populated only by the ions created by electron-impact ionization of the molecular Oxygen inside the sheath. As one can see in fig.2b increasing the neutral gas pressure, the ion-neutral collisions in the sheath start to dominate the shape of the IED, depleting the high-energy part and shifting the distribution toward lower energies. In fig.2c we present the experimentally measured IEDs [40]. As we can see, there is quite good agreement between the simulated and measured IEDs. One should mention that depletion of the sub-100 eV part of measured IEDs is caused by the limited sensitivity of the ion energy analyzer at this part of the spectrum.



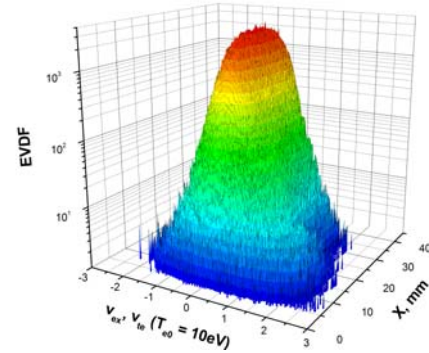
(a)



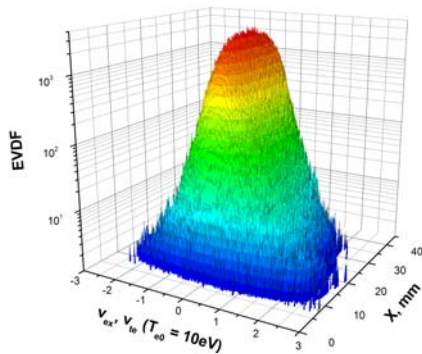
(b)



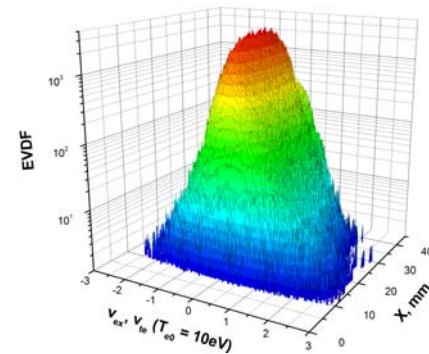
(c)



(d)



(e)



(f)

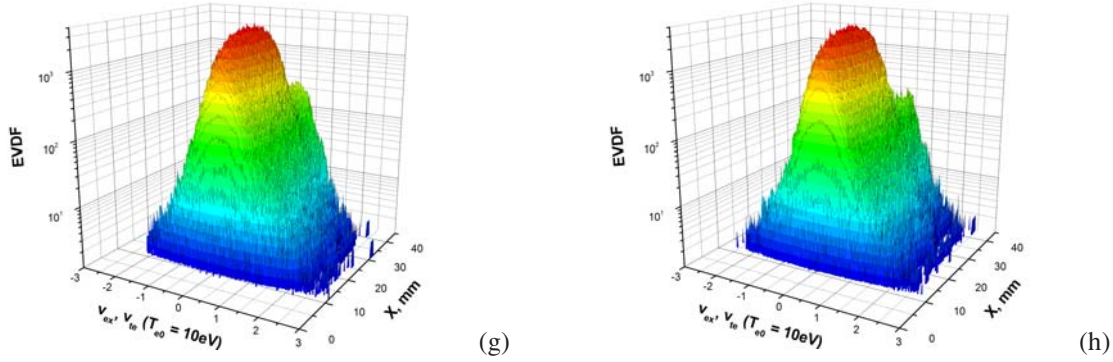


Fig. 3 Dynamics of the electron axial velocity component distribution during one RF cycle; $p = 5$ Pa, $U_{RF} = 1000$ V. The phase of RF cycle is: (a) $\varphi = -\frac{\pi}{2}$, (b) $\varphi = -\frac{3}{8}\pi$, (c) $\varphi = -\frac{\pi}{4}$, (d) $\varphi = -\frac{\pi}{8}$, (e) $\varphi = 0$, (f) $\varphi = \frac{\pi}{8}$, (g) $\varphi = \frac{\pi}{4}$, (h) $\varphi = \frac{3}{8}\pi$. (Online colour: www.cpp-journal.org).

In fig.3 we present profiles of the electron parallel velocity component v_x distribution function along the system, calculated at 8 different times during the half of RF half-period for $p = 5$ Pa and $U_{RF} = 1000$ V. The velocity is normalized to the electron thermal velocity $v_{te0} = \sqrt{\frac{kT_{e0}}{m_e}}$, calculated for $T_{e0} = 10$ eV. We can clearly distinguish two groups of electrons on these plots: the time-independent formation of cold electrons in the bulk, and the tail of high-energy electrons oscillating between the sheaths. As discussed in [20], the electrons in the low energy group (with average energy about 0.6 eV) are not energetic enough to overcome the ambipolar potential barrier and penetrate the sheath region, where they could be accelerated by the sheath electric field. Thus they are confined in the middle of the system. Eventually, due to elastic collisions, these electrons diffuse to the sheath regions, where they are accelerated in the strong sheath electric field. This group of electrons is mostly populated by the low-energy secondary electrons, produced in electron-neutral ionization collisions.

Unlike the electrons from the low-temperature group, the electrons from the high-energy tail can overcome the ambipolar potential barrier and penetrate into the region of strong electric field in the sheaths. As for 5 Pa the mean free path for electron-neutral elastic collisions $\lambda_{en} \sim \frac{1}{n_n \sigma_{en}} \approx 1.2$ cm is the same order of magnitude as the system length, these electrons can oscillate between the RF sheaths, getting reflected from them by the strong retarding electric field. Although during single reflection from the sheath, an electron can both gain and loose energy, depending on the phase of the RF field, on average, electrons can be accelerated due to stochasticization of their motion, following the Fermi acceleration mechanism [41]. Randomization of electron motion in RF discharges can also arise due to electron-neutral collisions. Collisions with neutrals become the only randomization mechanism, when condition for dynamic stochasticity is not satisfied [41, 42]. Such collisional randomization can be responsible for stochastic heating of electrons by RF sheaths even in case of low collisionality: $\lambda_{en} \gg d$ [41, 42]. As in our case $\lambda_{en} < d$, thus collisions with neutral gas should play dominant role in the randomization of electron motion and hence the stochastic heating.

In fig.4 we present the time-averaged electron energy probability function (EPPF), calculated in the middle of the system. The EPPF is defined as:

$$F_e(E) = 4\pi\sqrt{2}/m_e^{3/2} f_e\left(\sqrt{\frac{2E}{m_e}}\right), \quad (1)$$

with normalization:

$$\int_0^\infty F_e(E) \sqrt{E} dE = n_e. \quad (2)$$

Here $f_e(v)$ is the electron velocity distribution function, E and n_e – electron energy and local density respectively. As we can see the electron distribution can be quite well represented as a superposition of two Maxwellian

distributions with temperatures $T_1 = 1.2$ eV, $T_2 = 5.6$ eV. The low temperature part corresponds to the group of cold electrons in the bulk region, whereas the high-temperature component is contributed by the energetic electrons, oscillating between the sheaths. Such bi-Maxwellian electron energy distributions, corresponding to regime of stochastic heating were experimentally found in low-pressure capacitive RF discharges [20, 11, 43].

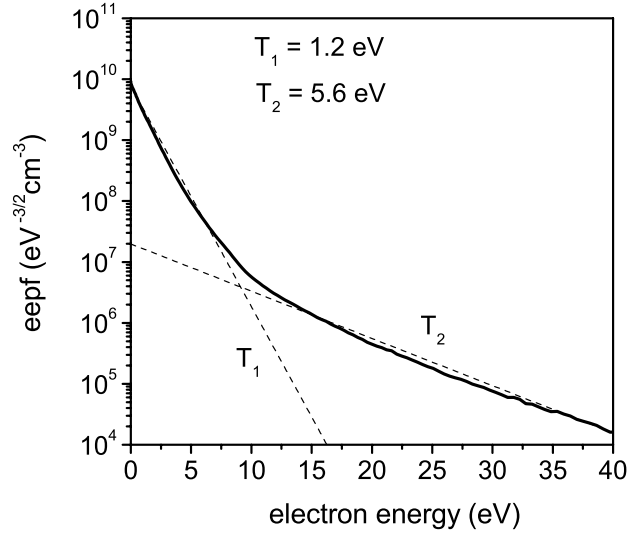


Fig. 4 The EEPF at the discharge mid-plane, averaged over RF cycle; $p = 5$ Pa, $U_{RF} = 1000$ V.

In order to investigate the dependence of the electron heating mechanism on the collisionality with the neutral gas, we performed simulations for the different background gas pressures. In fig.5 we summarize these simulations, presenting EEPF's averaged over the RF cycle in the bulk plasma for gas pressures 2 Pa, 5 Pa, 10 Pa, 20 Pa and 50 Pa. As we can see, at low pressures the EEPFs are essentially bi-Maxwellian, revealing the stochastic electron heating mechanism, leading to the formation of cold bulk and oscillating hot tail electrons. With increase of the neutral gas pressure between 20 Pa and 50 Pa EEPF transforms Druyvesteyn-type distribution, corresponding to a regime when the Ohmic heating in the sheath regions is the dominant mechanism of the electron heating as proposed by [20].

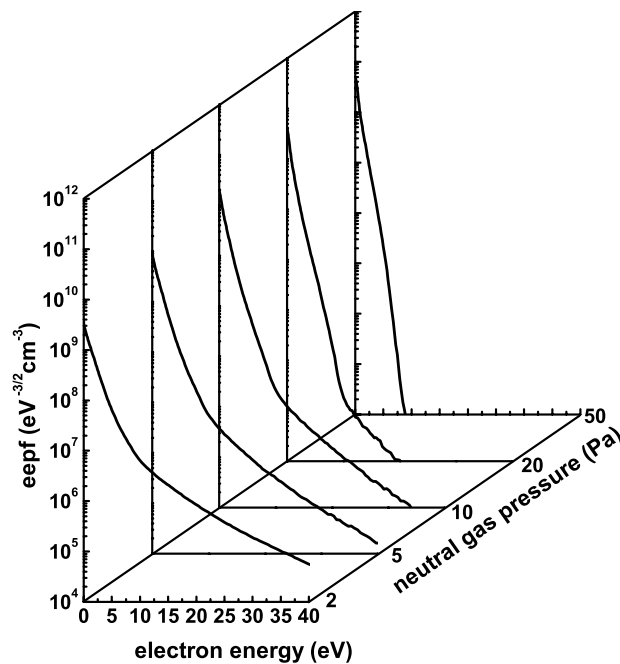


Fig. 5 The EEPF evolution with neutral gas (Oxygen) pressure.

During the experiments in the 20 – 60 Pa pressure range [5] an interesting phenomenon was observed. The optical light emission at 844 nm from the powered electrode was separated in two layers. The first one, highly modulated with RF frequency layer, was observed about 5 mm from the powered electrode, while the second one, being modulated only slightly was seen almost directly at the powered electrode. In fig.6 we present the spatio-temporal profile of the 844 nm atomic Oxygen emission line, corresponding to the $3p^3P \rightarrow 3s^3S$ transition [5]. The origin of the RF modulated optical emission about 5 mm from the electrode is quite clear. This emission is caused by the electron-impact dissociative excitation of the corresponding atomic Oxygen levels. Indeed, at these pressures the mean free path of electron-neutral elastic collision becomes smaller than the sheath length, so electrons get their energy in the oscillating sheath electric field between successive elastic collisions with the neutral gas, i.e. Ohmic heating is taking place [1].

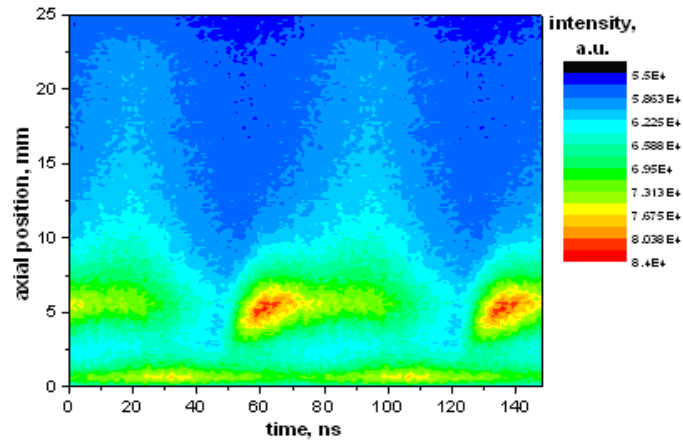
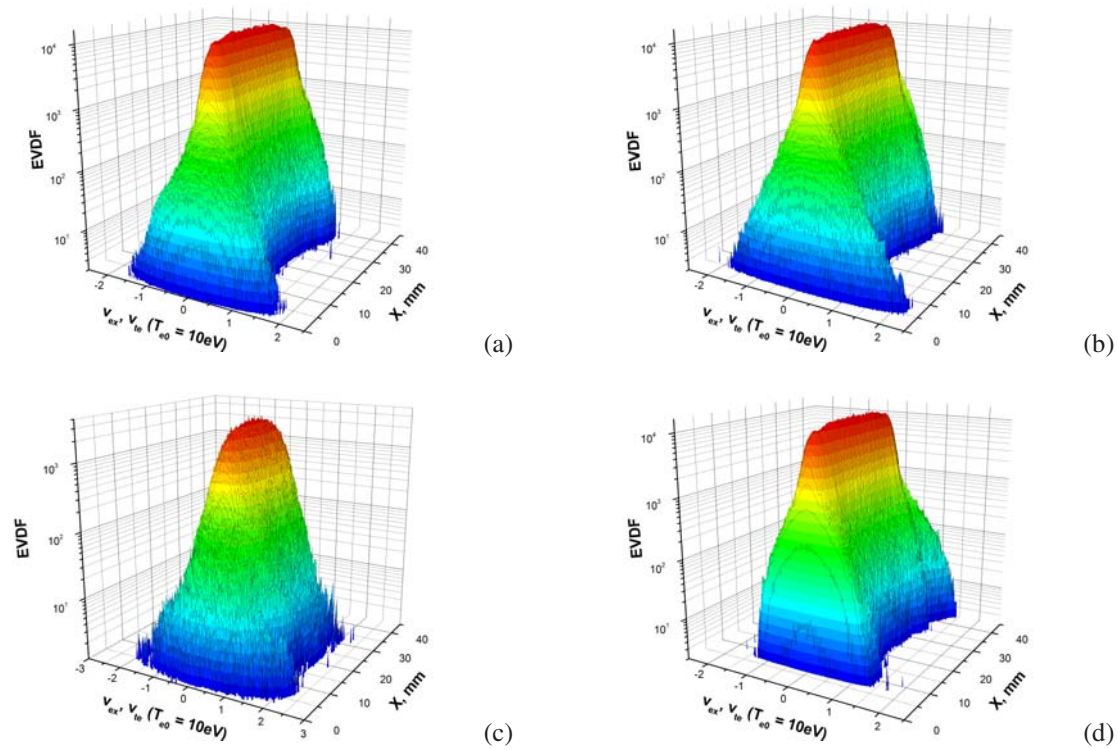


Fig. 6 Double emissive layer from experiment (844 nm). (Online colour: www.cpp-journal.org).



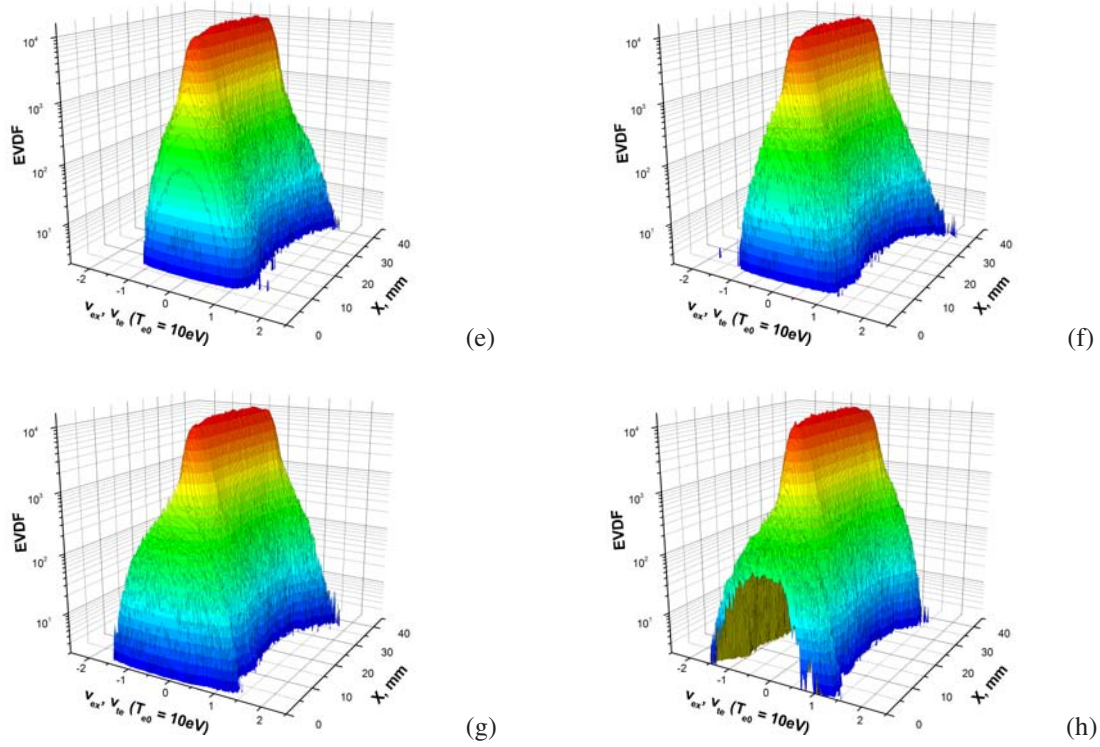


Fig. 7 Dynamics of the electron axial velocity component distribution during one RF cycle; $p = 60$ Pa, $U_{RF} = 800$ V. The phase of RF cycle is: (a) $\varphi = -\frac{\pi}{4}$, (b) $\varphi = 0$, (c) $\varphi = \frac{\pi}{4}$, (d) $\varphi = \frac{\pi}{2}$, (e) $\varphi = \frac{3}{4}$, (f) $\varphi = \pi$, (g) $\varphi = \frac{5}{4}\pi$, (h) $\varphi = \frac{3}{2}\pi$. (Online colour: www.cpp-journal.org).

In fig.7 we present the 8 profiles of the electron axial velocity component distribution from the simulation, corresponding to different phases of the RF cycle for $p = 60$ Pa, $U_{RF} = 800$ V. As we can see, high energy tails in the electron velocity distribution (EVD) are emerging only when the growing sheath is pushing the electrons away from the electrode (a), (b) and (c) in fig.7. The electrons reach the maximum energy close to the sheath entrance at about 5 mm from the electrode. These high-energy electrons are responsible for the majority of inelastic electron-neutral processes: ionization, dissociation and excitation.

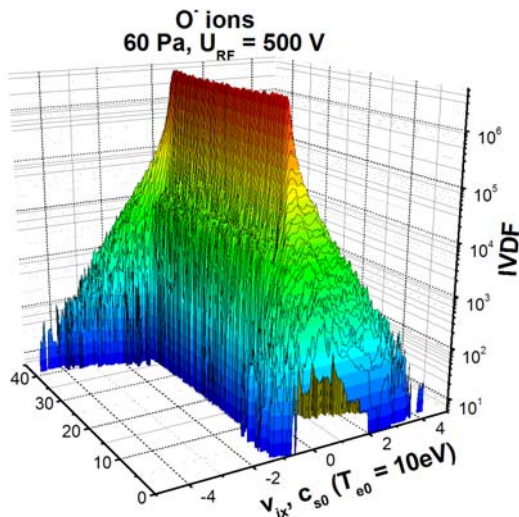


Fig. 8 O^- velocity distribution, averaged over RF cycle. (Online colour: www.cpp-journal.org).

An additional characteristic of such discharges is the creation of negative oxygen ions. In fig.8 we plot the O^- ions axial component distribution, averaged over the RF cycle for $p = 60$ Pa and $U_{RF} = 500$ V. We can see that negative ions, produced in the sheath are accelerated towards the bulk through the sheath electric field. They reach their maximum energy about 4 mm from the electrode. Further away they are very quickly cooled down to thermal energies of the neutral background gas due to elastic collisions with Oxygen molecules. The mean free path for such collisions at 60 Pa is extremely short $\lambda_{O-O_2el} \approx 0.4$ mm.

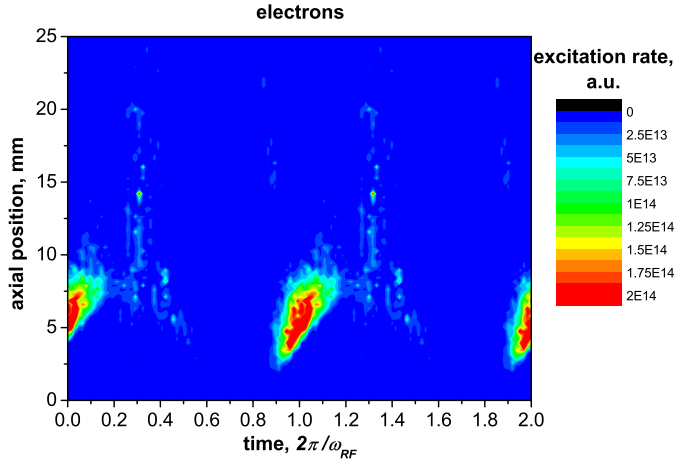


Fig. 9 Spatio-temporal distribution of the electron-impact excitation of 844 nm line; $p = 60$ Pa, $U_{RF} = 800$ V. (Online colour: www.cpp-journal.org).

In fig.9 we present the spatio-temporal profile of the electron-impact dissociative excitation of atomic Oxygen $3p^3P$ level from the simulation. As one would expect from the electron dynamics, the excitation takes place 3-7 mm away from the electrode during the first quarter of the RF cycle (b) and (c) in fig.7. But there is no evidence of an excitation process closer to the electrode as seen in the experiment [5]. This is not really surprising, because, as one can see in fig.7, no energetic electrons are reaching the electrodes. The electrons are able to reach the electrode only during a short time (h) in fig.7 to balance the ion current constantly flowing on the electrode. For the rest of the RF cycle there are no electrons near the electrode. While the energetic electrons are responsible for the RF modulated optical emission (located about 5 mm away from the electrode) the emission layer closer to the electrode needs another explanation.

The dissociative excitation of atomic Oxygen by energetic O_2^+ ions is the most plausible channel for this feature. Indeed, the ions get their maximum energy at the electrode, after crossing the sheath. The ion energy distribution close to the electrode is changing only slightly during the RF cycle, because the ions are too heavy to respond to the fast changing sheath electric field.

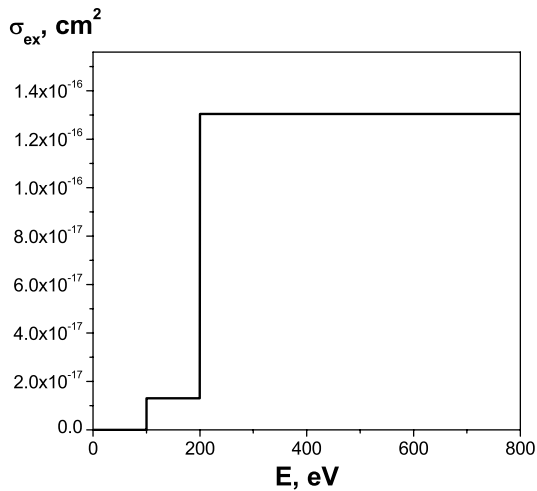


Fig. 10 Effective cross-section for $O_2^+ + O_2 \rightarrow O(3p^3P) + X$.

The only problem is that, to our knowledge, there are no data reported on ion- neutral inelastic collisions in Oxygen. We introduced the $O_2^+ + O_2 \rightarrow O(3p^3P) + X$ dissociative excitation process into the model. Here, the X expresses the fact that we are summing up all possible production channels of $O(3p^3P)$ excited state. Taking into account that in the experiments the emission from the electrode appears for self-bias voltages higher than 100 V, we set the threshold energy for this process to 100 eV. Starting with a one-step fit the relative height of electron and ion peak for $\tilde{U}_s = 327$ V was reproduced for a value $\sigma_{ex,1} = 1.3 \cdot 10^{-17} \text{ cm}^2$. Analyzing the variations of these peaks with RF voltage, a second step was introduced into the cross-section (see fig.10) and a reasonable agreement between experiment and modeling was obtained. The energy of the second step was chosen to reproduce strong jump in the intensity of the ion peak at higher RF voltages and a value of $\sigma_{ex,2} = 1.3 \cdot 10^{-16} \text{ cm}^2$ was adopted.

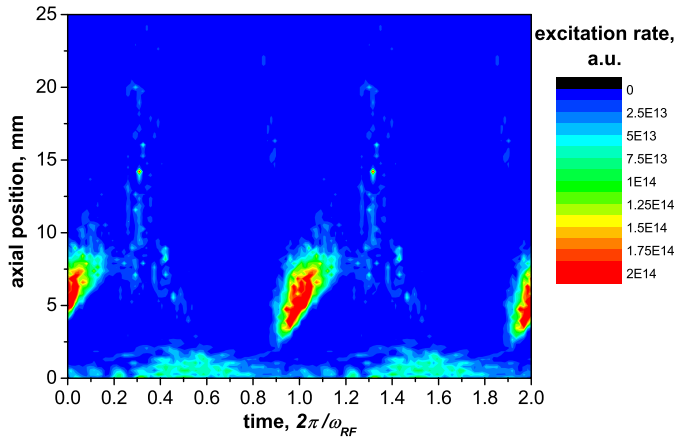


Fig. 11 Spatio-temporal distribution of the excitation of 844 nm line; $p = 60$ Pa, $U_{RF} = 800$ V. (Online colour: www.cpp-journal.org).

In fig.11 we present the spatio-temporal profile of the dissociative excitation of $O(3p^3P)$, summing up both electron and ion channels. As we can see, the addition of the ion channel resulted in a slightly modulated excitation layer very close to the electrode surface. The overall excitation pattern is very similar to the double layer emission structure from experiment (fig.6). When comparing the excitation profile from the simulation with the experiment, one should take into account that in experiment the emission profile is measured. Finite life-time effects on the excited $O(3p^3P)$ level will lead to formation of a wake-like structure extending the signatures for longer times (as seen in fig.6). In fig.12 (right panel) we present the results for the axial profile of the total excitation rate averaged over one RF cycle for different average sheath voltages. Comparing with the experimental measurements [5], presented in fig.12 (left panel), one can see rather good agreement.

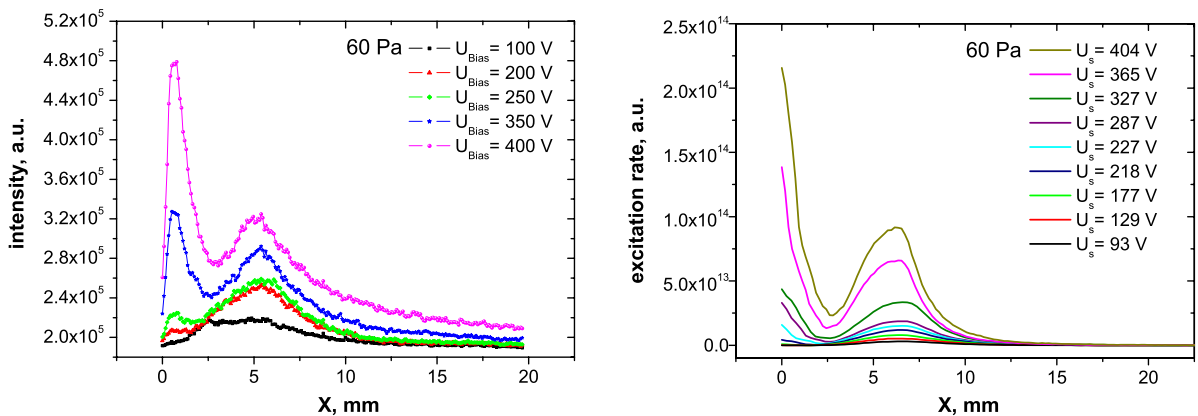


Fig. 12 RF cycle averaged experimental axial profile of 844 nm emission (left). Total $O(3p^3P)$ excitation rate simulated with PIC (right). (Online colour: www.cpp-journal.org).

3 Particle simulation of Dusty Plasmas

3.1 Introduction

In this chapter, we discuss PIC MCC simulation of dusty or complex plasmas. The interest in dusty plasmas was initially formed in the astrophysics community, as such plasmas are omnipresent in space including interstellar clouds, comet tails, planetary rings, etc [44, 45]. Later, such plasmas were found in plasma technology devices used for semiconductor manufacturing, where they are formed either due to gas phase reactions or due to plasma-surface interaction. In semiconductor manufacturing and other surface modification technologies formation of the dust in the plasma reactor leads to contamination of the processed surface and as a result affects the quality of produced devices and reduces the efficiency of technological process [46]. The negative technological impact of dusty plasmas triggered research work on such plasmas in the plasma physics community [47, 48]. As a result of increased knowledge and the ability to control the particles in the plasma new applications for dusty plasmas were found [47]. Nowadays such plasmas are successfully used for producing new materials, where incorporation of the nano- or micro-particles in the growing surface helps to produce materials with new properties. Production of ultraflexible ceramic materials [49], polymorphous silicon films for optoelectronic devices with higher efficiency [50] and a new generation of solar cells [51] may serve as examples of technological application of dusty plasmas.

In nuclear fusion research formation of dust inside magnetic confinement fusion devices receives growing concern [52-55]. Dust can be formed inside the fusion device due to erosion of plasma facing components and soft co-deposited carbon layers. Since such carbon particles can retain large amounts of hydrogen, dust contributes to the problem of inventory of radioactive tritium inside the fusion machine. Another impact of the dust particles in the operation of a fusion device is the possible degradation of the discharge performance. Such particles penetrating in the core plasma region can lead to discharge disruption [56]. Thus, in order to perform successful fusion experiments it is important to assess and understand the processes by which dust is formed and by which it interacts with the fusion device and its plasma.

In low-temperature laboratory plasmas the absorption of electrons and ions is the dominating mechanism of micro-particles charging. In such plasmas a dust particle acts as a small floating probe, receiving the net negative charge due to higher electron mobility. As a result, a particle acquires a negative floating potential which repulses the electrons and accelerates the ions, balancing electron and ion currents to the particle. The typical charge of micrometer sized particles in laboratory plasmas is of the order of 10^4 elementary charges. Despite the large electric charge, the charge to mass ratio for such particles remains very small, much smaller than that of ions. Due to their big mass and size the dust particles in the complex plasmas are subject to a variety of forces, which are unimportant in usual plasmas [44, 57]. Because of small charge to mass ratio the gravitational force becomes dominating for such particles, being comparable or even larger than electrostatic forces resulting from the plasma electric fields. Collisions of the dust particles with the residual gas atoms or molecules lead to a neutral gas friction force, damping the particle motion. Momentum transfer due to collection and Coulomb scattering of the ions gives rise to the ion drag force, which in certain cases can strongly influence the particle behavior [58].

In capacitive RF discharge the gravitational force acting on the particles can be equilibrated by the electrostatic force due to a strong repulsive electric field in the RF sheath. In this case particles are trapped in the discharge and form a cloud levitating above the lower electrode. The dust particles interact with each other through the repulsive Coulomb potential, screened by the plasma electrons and ions. In the case of strong electrostatic coupling, i.e. when the energy of the interparticle interaction is large compared to the particle thermal energy, particles self-assemble into ordered structures, known as Coulomb (plasma) crystals. The possibility of Coulomb crystallization of micrometer-sized particles in low-temperature laboratory plasmas was first theoretically predicted by Ikezi in [59]. Later, the plasma crystals were observed in laboratory plasma experiments: [60-64].

Such strongly coupled dust structures may serve as a unique model system for studying the physical processes in condensed matter, such as phase transitions [65, 66], waves and oscillations [67-69], Mach cones [70, 71], etc. Due to the large mass of the dust particles the characteristic relaxation time for the plasma crystals is usually of the order of seconds, making such structures easy to observe with ordinary video-observation techniques. The inter-particle distance in dusty plasma crystals is usually of the order of a fraction of millimeter, so that it is possible to observe such structures even with a naked eye. The plasma crystals represent a bridge connecting the atomic or molecular scale of matter with the macroscopic scale of a dusty particle system, giving a unique possibility to observe the processes in the condensed matter on the kinetic level.

Despite considerable interest to the subject, the number of the sophisticated simulations for the dusty plasmas is still rather limited. The reason is the complexity of the model required to simulate such systems. The discharge plasmas used for confinement of the dust (usually capacitive RF discharges are used for this purpose), are dominated by the kinetic effects. Such effects have to be resolved accurately, in order to correctly determine the fluxes of the plasma particles close to the dust grains, as these fluxes define the important dust quantities: charge, potential, ion drag force due to momentum transfer from the ions. Huge difference in time scales for the plasma and the dust particles dynamics makes the simulation of such system even more complex.

In [72-75] dust particles dynamics in capacitive RF discharge was studied using a fluid approximation for the background plasma.

Goedheer *et al.* used a one dimensional PIC code to follow electrons and ions, while the dust density profile was fixed [76]. The charging of the dust was included in the model by means of the Orbital Motion Limited (OML) expressions [77] for the capture cross section.

Hutchinson applied a two dimensional PIC model, in which the ion dynamics was resolved and Boltzmann electrons were considered, to quantify the dust charge, floating potential and ion drag force for spherical dust particle immersed within a background flow of Maxwellian ions [78-81].

In [82] dynamics of the spherical dust particle in the divertor plasma was studied with a two dimensional PIC MCC code. This model can be applied only for the "large" size dust particles $R_d > \lambda_D \sim \Delta x$, so that the electric field at the dust surface can be directly calculated from the surface charge, accumulated on the dust. Condition $R_d > \Delta x$ is also necessary to satisfy the intrinsic resolution limit Δx of the PIC algorithm.

Vladimirov et al used a 3D kinetic model to study the dust charging and wake-field formation for a single dust particle [83] and a pair of dust particles [84] in the prescribed stationary ion flow. The interaction between the plasma particles and the dust was accounted through the direct particle – particle Molecular Dynamics approach, which limited the computational domain size to $\sim 40 \mu m$ and the simulated time to $\sim 10^{-8} s$.

We present the results of the 2D and 3D PIC MCC simulation of dusty plasmas, confined in the capacitive RF discharge. The simulation features the full-scale self-consistent kinetic model of capacitive discharge as background plasma. In subsection 3.2 we investigate formation of the ordered structures and the influence of the dust on the parameters of the discharge plasma. Here, dust particles are introduced in the model as additional charged species with a fixed charge. In order to study the charging of the dust particle self-consistently, we have developed a 3-dimensional Particle-Particle Particle-Mesh (P³M) model. In the model, the long-range interaction of the dust grains with charged particles of the background plasma is treated according to the PIC formalism. If particles are closer to the dust grain than a Debye length, their interaction force is computed according to a direct particle-particle MD scheme using the exact Coulomb potential. This approach allows to follow the plasma particle trajectories in the close vicinity of the dust grain and by this to include finite-size effects for dust grains. Thus, the dust grain charging due to collection of plasma electrons and ions is resolved in a self-consistent manner. In the subsection 3.2, the P³M model is described and results of 3-dimensional simulation of the charging process of micrometer size dust grains confined in a capacitive RF discharge are presented.

3.2 2d and 3d PIC simulations of dusty plasma in capacitive RF discharge

In this work we study the formation of dust structures in a capacitive coupled RF discharge. As a first step, a particle-in-cell (PIC) code with Monte-Carlo collisions (MCC) resolving 2 spatial dimensions and 3 velocity components [85] was used. The dust particles were introduced into the model as additional charged species, using the Cloud-in-Cell weighting formalism [86], so that no finite size effects for dust particles were considered. In addition to the electrostatic force the gravitational and neutral gas friction forces were also considered for the dust particles. The equation of motion of a dust particle is:

$$\frac{d\vec{v}}{dt} = \frac{q_d}{m_d} \vec{E} + \vec{g} - \beta \vec{v}, \quad (3)$$

where q_d and m_d are particle charge and mass, g is gravitational acceleration and β is the normalized friction coefficient.

As a background gas, methane with concentration $n_{CH_4} = 7 \cdot 10^{14} \text{ cm}^{-3}$ and temperature $T_{CH_4} = 500 \text{ K}$ was used. The initial electron density and temperature were chosen as $n_{e0} = 2.5 \cdot 10^9 \text{ cm}^{-3}$ and $T_{e0} = 10 \text{ eV}$ respectively. The computational domain is a rectangle in an XY plane, where the Y axis corresponds to the vertical

direction. The vertical size of the system is $Y_{\max} = 32\lambda_{D0} = 1.5$ cm and the width is $X_{\max} = 16\lambda_{D0} = 0.75$ cm. The lower electrode at $Y = Y_{\max}$ is grounded and the upper electrode at $Y = 0$ is powered with a sinusoidal voltage with frequency $f_{RF} = \omega_{RF}/2\pi = 13.56$ MHz. The neutral gas was treated as a fixed background with constant density and temperature. Only the charged particle dynamics was followed. In order to speed up the simulation, reduced masses of the ions and dust particles were used. The ion-electron mass ratio was set to $m_{CH_4^+}/m_e = 1600$. The mass of the dust particles was chosen as $m_d/m_{CH_4^+} = 640$, which gives the mass of the dust particle about 8 orders of magnitude smaller than in the laboratory experiments. In order to compensate for the decreased mass of the dust particles and match the gravitational force to the electrostatic force acting on particles in the RF sheath, the gravitational acceleration was increased by a factor of $5 \cdot 10^9$ compared to the real value. The constant charge of the dust particles $q_d = 5 \cdot 10^4 \cdot e$ was assumed (no charging processes were accounted for). The viscosity coefficient was set to $\beta = 1.4 \cdot 10^6 \text{ s}^{-1}$.

Such artificial modification of the system parameters allowed us to accelerate the computation to achieve an acceptable simulation time. The calculations were carried out on Linux cluster with 8 AMD Athlon 1800+ MHz processors in about 2 weeks.

In the beginning of the simulation the dust particles were randomly introduced in the middle of the system. After about 10^{-4} s they formed the cloud levitating about $2\lambda_{D0}$ above the lower electrode.

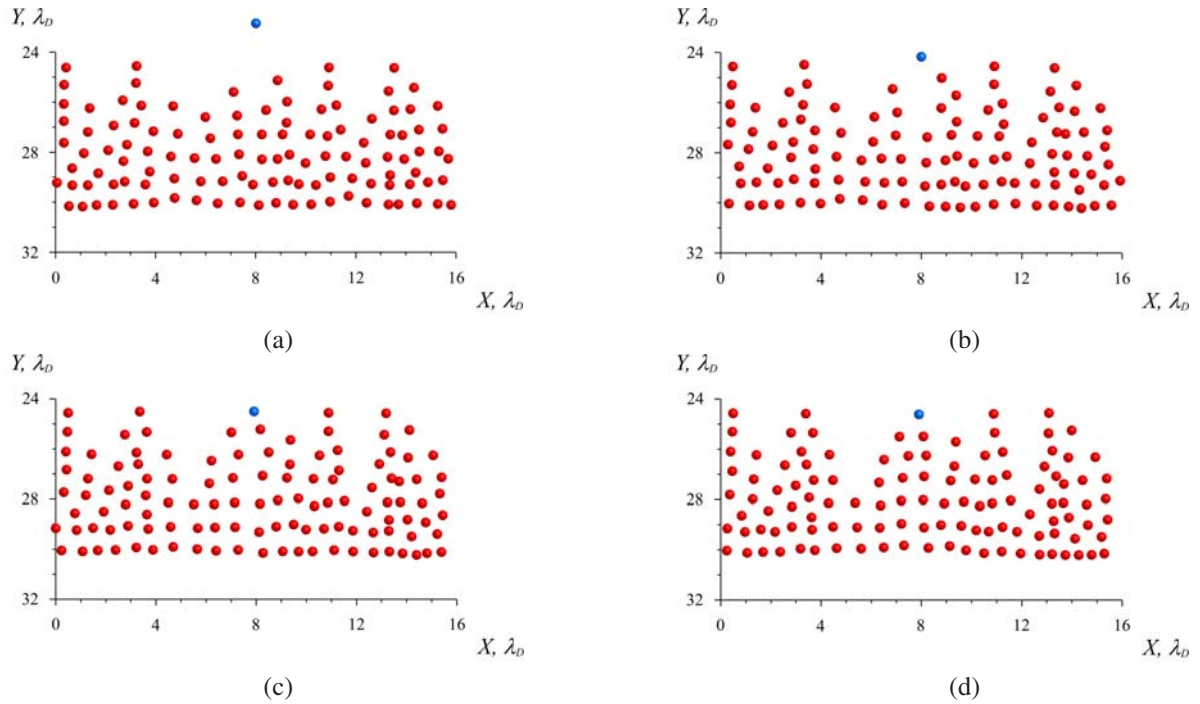


Fig. 13 Evolution of dust cloud above the lower electrode ($Y = 32 \lambda_D$). a) $t = 1.4 \mu\text{s}$, b) $t = 1.407 \mu\text{s}$, c) $t = 1.414 \mu\text{s}$, d) $t = 1.421 \mu\text{s}$.

In fig.13 we present the dynamics of a dust cloud plotting four particle distributions with a time interval of $7 \cdot 10^{-6}$ s. We can see that particles form a structure with several horizontal layers and interparticle distance of about one Debye length. The new particle (marked in blue) is added to the system. We can see how this particle joins the existing dust cloud structure above the lower electrode. When this new particle falls down, it approaches the cloud (fig.13a-b). The particles underneath change their horizontal position and align themselves in a vertical string-like structure under the newly added particle (fig.13d). We can see several such vertically aligned 'strings' of dust particles, so called 'dust molecules' in fig.13. These dust strings are rather stable, when the upper particle moves in a horizontal direction, the whole lower part of the particle string follows this motion, being attracted to the upper particle, so that the vertical alignment is conserved. Such attraction of negatively charged particles can not be explained on the basis of particle interaction through the isotropic Yukawa potential:

$\phi(r) = \frac{q_d}{4\pi\epsilon_0 r} \exp\left(-r/\lambda_D\right)$. Origination of such vertically aligned dust structures can be attributed to the positive wake-potential arising due to focusing of the ion flow by the negative dust particles [87]. Indeed, in the sheath region, where the dust particles are levitating, the ions are flowing with velocities close to or larger than the ion sound velocity. When the ion flow encounters the negatively charged dust particle it gets focused, forming an ion beam in the wake of the particle. The dust particles downstream are attracted to this ion beam, creating a vertical string of dust particles coupled with the focused ion flow. In fact, creation of such stable vertical dust structures in which like-charges are attracted to each other due to medium polarization is similar to the Cooper pairing of the electrons in superconductivity [87]. The physical idea of Cooper-pairing is that a test electron moving through the crystal lattice polarizes it attracting the positive ions. This positive ion wake attracts the second electron. If this attraction is strong enough to overcome the Coulomb repulsion of two electrons, the electron pair is formed and superconductivity results [88]. For effective attraction the speed of the electrons relative to the ion background should exceed the sound velocity. In the case of the dust strings, however the dust particles are static and the ion flow creates polarization necessary for particle attraction. Such stable vertical dust strings were observed in laboratory experiments [64] and obtained in the numerical simulations [89, 90]. The analytical models for wake-field potential of dust particles in the ion flow were developed in [87, 91].

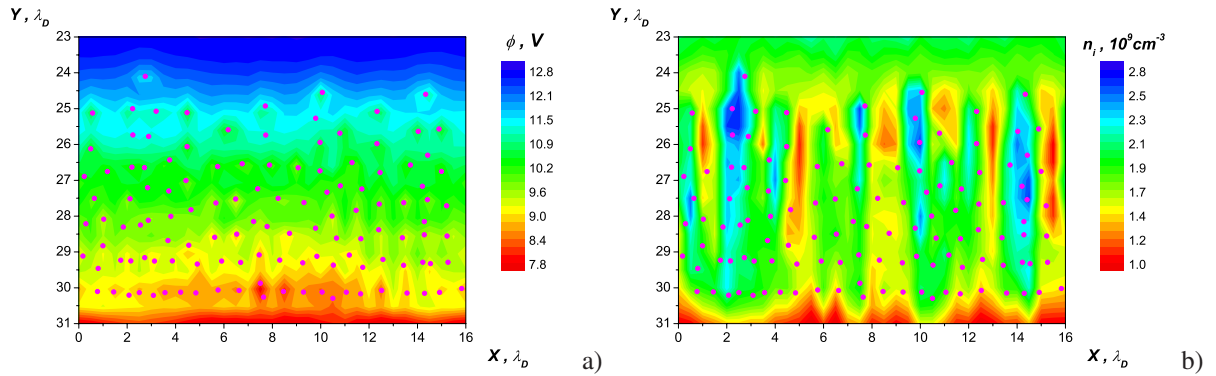


Fig. 14 Map of potential a) and the ion density b) averaged over RF cycle. Position of the lower electrode is $Y = 32 \lambda_D$. Positions of dust particles are marked as \bullet . (Online colour: www.cpp-journal.org).

In fig.14a we present the potential map near the lower electrode, marking the dust particle positions. We can note that the position of each dust particle corresponds to the local potential minimum. Strip-like structures in the potential along vertical dust strings can also be distinguished.

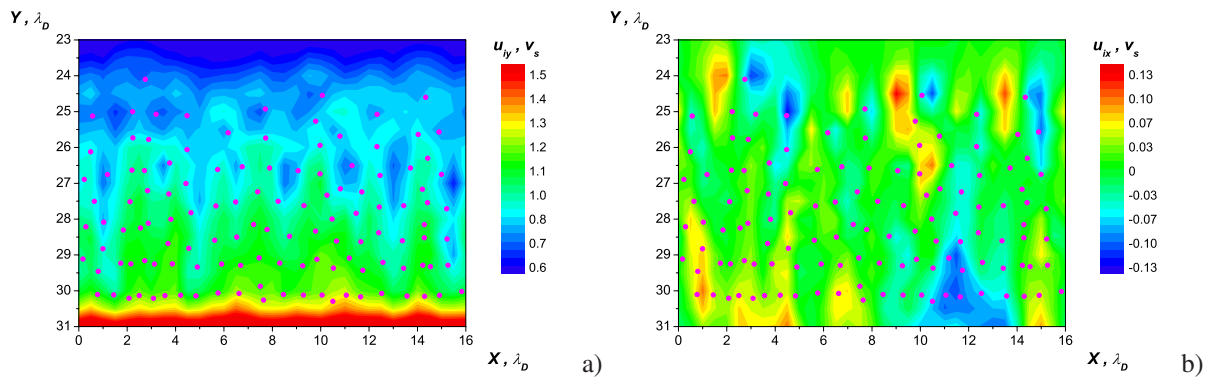


Fig. 15 Map of the vertical (a) and horizontal (b) component of ion velocity, averaged over RF cycle. (Online colour: www.cpp-journal.org).

In the fig.15a we present the map of the vertical ion velocity component. Here we can see how ions are accelerated in the sheath toward the electrode in the averaged RF potential. The vertical ion velocity follows the potential structure, showing the ion streams accelerated along the dust strings. We can see that in the dust layer

the ions become essentially supersonic. On the map of the horizontal component of the ion velocity in fig. 15b we can see how ion flow is focused by the upper dust particles. These focused ion flows aligned along the vertical dust strings can be seen in the fig. 14b, where the ion density is plotted. The density in the ion flow along the dust strings is a factor of 2 larger than its average value.

In order to model the formation of three-dimensional dust crystals, we performed full 3d particle simulation of the strongly coupled dusty plasmas in capacitive RF discharge. For this purpose the full 3d version of the PIC MCC code was developed. The plasma parameters were chosen similar to those used in the 2d model described above – the methane plasma with $n_{e0} = 2.5 \cdot 10^9 \text{ cm}^{-3}$, $T_{e0} = 10 \text{ eV}$, $n_{CH_4} = 7 \cdot 10^{14} \text{ cm}^{-3}$ and $T_{CH_4} = 500 \text{ K}$. The computational domain represents a 3d box with dimensions: $Y_{\max} = d = 32\lambda_{D0} = 1.5 \text{ cm}$, $X_{\max} = Z_{\max} = 8\lambda_{D0} = 0.38 \text{ cm}$, where Y corresponds to the vertical direction and d is the electrode spacing. The lower electrode at $Y = Y_{\max}$ is grounded and the lower at $Y = 0$ is powered. The electrodes act as an absorbing wall. Periodic boundary conditions were applied in the X and Z directions both for particles and for the potential. A grid with spacing $\Delta x = \Delta y = \lambda_{D0}/2 = 0.024 \text{ cm}$ and time step $\Delta t = 0.2/\omega_{pe} = 7 \cdot 10^{-11} \text{ s}$ was used in the simulation. The ion mass was reduced to $m_{CH_4^+}/m_e = 1600$. Dust particles with constant charge $q_d = 5 \cdot 10^4 \cdot e$ and mass $m_d/m_{CH_4^+} = 4.8 \cdot 10^7$ were assumed. The gravity was increased by a factor of $9 \cdot 10^8$. The viscosity coefficient in eq. (3.1) was set to $\beta\Delta t = 0.001$, which gives the characteristic time for a particle slowing down due to neutral gas friction $\tau = 1/\beta = 7 \cdot 10^{-8} \text{ s}$. The calculations were carried out on Linux cluster with 16 AMD Athlon 1800+ MHz processors in approximately one month.

At the beginning of the simulation the dust particles were injected into the discharge at random positions. After about 10^{-4} s particles were settled in an ordered structure above the lower electrode. In fig. 16 we present the dust structure equilibrated over the lower electrode of capacitive RF discharge with plasma parameters close to those used in 2D simulation. We can see that particles are divided in three horizontal layers with a separation of about one Debye length (for convenience we highlighted the layers with different colors).

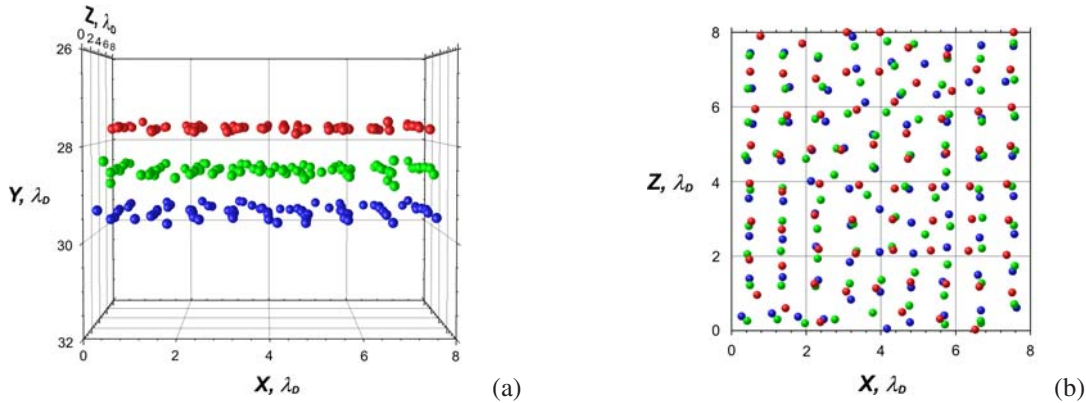


Fig. 16 Side (a) and top (b) view of 3D plasma crystal. (Online colour: www.cpp-journal.org).

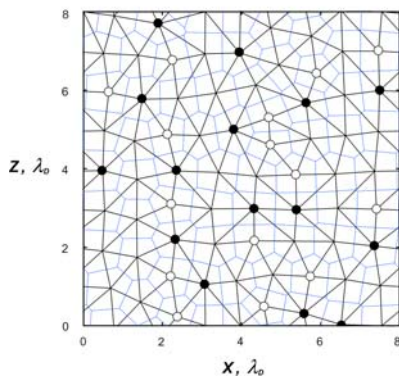


Fig. 17 Delaunay triangulation (black lines) and the Voronoi cells (blue lines) of the upper horizontal layer of the 3D crystal. (Online colour: www.cpp-journal.org).

When looking on the dust structure from above (fig.16b) we can note that particles tend to form 'triads', as particles belonging to three different layers are aligned vertically. This is the same type of alignment, observed for the 2-dimensional case, which is caused by the polarization of the ion flow in the sheath region. Thus the dust formation on fig.16 shows a quasi-two-dimensional structure of vertically aligned horizontal layers with a similar structure. We analyzed the upper particle layer using two-dimensional static structural methods. In the fig.17 we plot the Voronoi diagram for the upper dust layer, connecting the nearest-neighbor bonds identified using a Delaunay triangulation. As we can see from the Voronoi diagram the layer shows a rather distorted hexagonal structure pattern. On the Delaunay triangulation we marked each particle with seven close bonds with black circles, and particles with five bonds with blank circles, leaving the particles with six bonds unmarked. We can see that the hexagonal structure is prevailing, although with a number of defects. The pairs of neighboring particles with 5 and 7 close bonds form the numerous dislocation defects.

The temperature of the dust particles in the simulation was estimated as $T_d \approx 2\text{eV}$. We also calculated the Coulomb coupling parameter for the dust particles in the crystal, which is given by the ratio of the mean energy of Coulomb interaction between two particles to the particle thermal energy:

$$\Gamma = \frac{q_d}{4\pi\epsilon_0 r_d k T_d} \exp\left(-\frac{r_d}{\lambda_D}\right), \quad (4)$$

where r_d is the distance between the neighboring particles and k is the Boltzmann constant. In our case $r_d \approx \lambda_D$ and the coupling parameter is $\Gamma \approx 500$. This small value of Coulomb coupling parameter may explain the high level of disorder in observed crystal structure. Usually in laboratory experiments the well established crystalline structures were observed when $\Gamma \sim 10^3 - 10^4$ [65, 92]. The structure obtained in our simulation may correspond to the intermediate state described as 'vibrational' in [66, 93], which is characterized by a reduced order and the increased vibrational temperature of the particles.

The vertically aligned horizontal layers with a flat hexagonal symmetry form the simple hexagonal structure. Such structures can not be obtained with particles interacting through the isotropic potential. For isotropic potential the close-packed three-dimensional structures, like face-centered cubic (fcc) and body-centered cubic (bcc) are energetically more favorable [64]. The origin of the simple hexagonal structure may only be explained by the symmetry braking with the attractive wake fields, arising from the focusing of the ion flow below the dust particles. This ion flow attracting the downstream particles leads to the vertical alignment of the particles of the lower layers. In the horizontal plane the potential remains symmetrical, thus a flat hexagonal structure, which is the minimum energy state for a two-dimensional symmetric potential is developing.

Such quasi two-dimensional dust crystal structures with simple hexagonal structure were observed in laboratory experiments with plasma crystals [64, 65].

3.3 Effect of grain size on dust charging in an RF plasma

The charge on the dust particles in a dusty plasma is a crucial parameter for the formation of Coulomb crystals, their structure and their dynamics. We apply a 3-dimensional Particle-Particle Particle-Mesh (P³M) code to investigate the charging process of micrometer size dust grains confined in a capacitive RF discharge. In our plasma model, plasma particles (electrons and ions) are treated kinetically (Particle-in-Cell with Monte Carlo Collisions (PIC-MCC)), which allows to self-consistently resolve the electrostatic sheath in front of a wall.

In order to accurately resolve the plasma particles' motion close to the dust grain, when plasma electrons and ions approach to the dust grain close than a Debye length, we compute their interaction force according to a direct particle-particle scheme using the exact Coulomb potential. This approach allows to follow the plasma particle trajectories in the close vicinity of the dust grain and by this to include finite-size effects for dust grains. Thus, the dust grain charging due to collection of plasma electrons and ions is resolved in a self-consistent manner.

Here, the charging of dust grains in a capacitive RF discharge and its dependence on the size and position of the dust is investigated. The results are compared with laboratory measurements.

As discussed before we have studied the formation of dust structures in low temperature laboratory plasmas with a self-consistent particle simulation [94, 95]. Although PIC simulations proved to be a powerful tool for studying dusty plasmas, the PIC method has a considerable drawback. As discussed in the first paper of this series, the spatial resolution in the PIC scheme is limited by the size of the grid which is typically of the order of the Debye length (fraction of a millimeter for low temperature plasmas). The size of the dust grains is typically

in the micrometer range and thus much smaller than the grid size. In conventional PIC algorithms, the particles are represented by charged clouds of the grid size and are able to penetrate each other [86]. This leads to high inaccuracies for interparticle interaction when the distance becomes smaller than the cell size. In this case the interaction force is strongly deviating from the Coulomb force for small distances and tends to go to zero as the interparticle distance decreases (see fig. 6 in the first paper).

Therefore, conventional PIC models are able to resolve long range (larger than the Debye length) interaction between the particles, but fail to resolve the close-range interaction for distances comparable with the radius of the dust grains.

In order to accurately resolve close-range interactions between dust grains and plasma particles, we extended our PIC model, combining it with the molecular dynamic (MD) algorithm. In the resulting Particle-Particle Particle-Mesh (P³M) model, the long-range interaction of the dust grains with charged particles of the background plasma is treated according to the PIC formalism. For particles which are closer to the dust grain than a Debye length their interaction force is computed according to a direct particle-particle MD scheme using the exact Coulomb potential. This is implemented in the following way: in the computational domain, the cell in which the dust grain is located together with the neighboring cells form the "MD" region. All particles outside the MD region are treated according to the conventional PIC scheme. For plasma particles (electrons and ions) inside the MD region the electric field is calculated as: $\mathbf{E} = \mathbf{E}_{grid} + \mathbf{E}_{dust}$. For the calculation of the grid field \mathbf{E}_{grid} we use the charge density as in the PIC part from which the dust grain contribution is subtracted. The dust contribution is accounted for by the exact Coulomb electric field \mathbf{E}_{dust} . In order to resolve particle motion on scales of the order of the dust grain size, particles in MD region are moved with time step smaller than in the PIC region. Plasma particles which cross the computational dust grain boundary are assumed to be absorbed. The dust grain charge is updated each MD time step.

We have applied the P3M model to investigate the dust grain charging process in a capacitive RF discharge in the argon. The parameters of the simulation were chosen to represent the conditions of the experiments with Coulomb balls (see Ref. [96]). As a background gas, argon with a pressure $p = 50$ Pa and temperature $T_{Ar} = 300$ K was used. The initial electron density and temperature were chosen as $n_{e0} = 1 \cdot 10^9 \text{ cm}^{-3}$ and $T_{e0} = 2.5$ eV respectively.

The computational domain represents a 3D box with dimensions: $X_{max} = d = 64\lambda_{D0} = 2.38$ cm, $Y_{max} = Z_{max} = 4\lambda_{D0} = 0.15$ cm, where X corresponds to the vertical direction and d is the electrode spacing. The lower electrode at $X = 0$ is grounded and the upper electrode at $X = X_{max}$ is powered with a sinusoidal voltage with frequency $f_{RF} = \omega_{RF}/2\pi = 13.56$ MHz and the amplitude $U_{RF} = 50$ V. At the electrodes absorbing wall boundary conditions for the particles are applied. At boundaries in the Y and Z directions periodic boundary conditions are applied, both for particles and the potential. The neutral argon was treated as a fixed background with constant density and temperature. Only the charged particle dynamics was followed. Coulomb collisions between charged species, electron-impact ionization, efficient excitation, electron-argon elastic collisions and momentum transfer charge-exchange collisions were taken into account in the simulation. A grid with spacing $\Delta x = \Delta y = \Delta z = \lambda_{D0}/2 = 0.019$ cm and time step $\Delta t = 0.2/\omega_{pe} = 1.21 \cdot 10^{-10}$ s was used. In the simulation, the plasma was sustained self-consistently due to electron impact ionization of the neutral gas by the electrons accelerated in the applied RF voltage.

Dust particles with radii $R_d = 1.86, 3.72, 7.44, 11.16$ and $14.88 \mu\text{m}$ were introduced into the discharge with zero starting charge. The position of the dust particles was fixed at four different positions: dust grain in the sheath $X_d = 8.5\Delta x$, at the sheath border $X_d = 24.5\Delta x$ and in the bulk $X_d = 40.5\Delta x$ and $X_d = 56.5\Delta x$. In all cases $Y_d = Z_d = 3.5\Delta y$. During the simulation the dust grains acquired a negative charge by the collection of plasma electrons and ions.

In fig.18 we present the evolution of the electric charge of a dust grain with a radius of $3.72 \mu\text{m}$ at $X_d = 56.5\Delta x$. A fast initial charging takes place due to the collection of electrons, while equilibration takes place on the ion time scale (of the order of microseconds). The equilibrium dust charge is subject to stochastic fluctuations due to the discrete nature of charge carriers (in the simulation one computational particle represents 171 real electrons or ions).

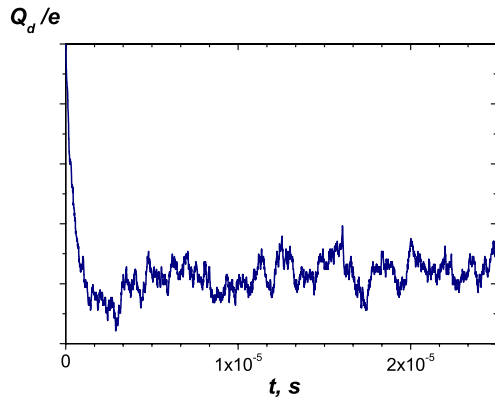


Fig. 18 Charging of a dust grain with a radius of $3.72 \mu\text{m}$ in the bulk of a capacitive RF discharge.

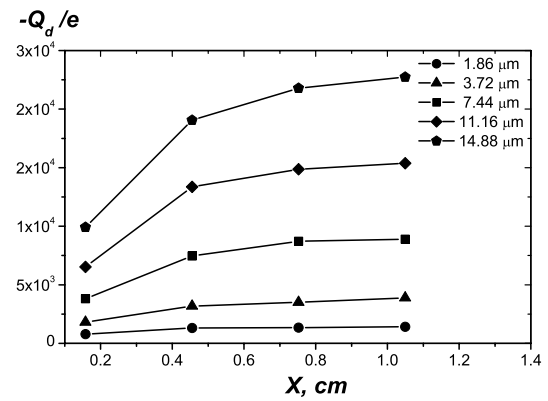


Fig. 19 Dependence of the dust grain charge on the radius and the axial position.

In fig.19 the dust charge as a function of position in the discharge is shown for dust grains of different radius. It is seen that the charge number is reduced in the sheath and at the sheath edge compared to the bulk value. This is due to the reduced electron flux to the dust particles near and in the sheath. The dust charge scales roughly linearly with the dust radius as expected from the capacitor model. The dust charge from the simulations is decisively (around factor 5) smaller than calculated from the simple collisionless OML model, but is in general reasonable agreement with experiments [65, 96]. In experiments on Yukawa balls with particles of $1.7 \mu\text{m}$ radius a charge of about 2000 is found [96], whereas the simulations yield 1400 charges for a particle of $1.86 \mu\text{m}$. From melting experiments, a charge of about 9000 is measured for a $4.7 \mu\text{m}$ radius particle [65]. Here, the simulations suggest a value of about 6000.

4 PIC modeling of negative ion sources

4.1 Introduction

Negative hydrogen (H^-) ions have a wide range of applications, e.g., for generation of intense neutral beam (NB) for heating magnetically confined fusion plasmas, for intense H^- injection into cyclical accelerators, and for plasma processing, such as for the de-lamination of Si wafer for silicon on material technology. These applications provide a strong impetus for the development of H^- sources with increasing extracted beam intensities, better beam optics and higher duty factors.

For fusion applications, the following two types of discharge plasmas are mainly used to produce H^- ions: multicusp arc-discharge plasma source and radio frequency inductively coupled plasma sources. In the former, electrons are emitted from hot filaments. The wall acts as the anode for the electron discharge. Plasma is confined by multi-cusp magnetic fields. On the other hand, RF coils are used to generate the plasma in the latter type sources. H^- ions are produced through volume reactions and/or Cs-seeded wall-surface reaction processes in these discharge plasma sources.

Reactor relevant fusion reactors like ITER require a N(negative)-NBI system with 1) high H^- beam current ($\sim 10\text{--}40 \text{ A}$), 2) high beam energy ($\sim 500\text{keV--}2\text{MeV}$), 3) long pulse operation ($\gtrsim 1000\text{s}$), 4) low beam divergence ($\lesssim 5\text{mrad}$), 4) low electron beam current (ratio of electron current to negative ion current: $I_e/I_{\text{H}^-} < 1$) and 5) spatial uniformity of extracted beam current. Therefore, key R&D issues for H^- ion sources in fusion applications are: 1) efficient H^- ion production in low gas pressures ($\lesssim 0.3\text{Pa}$), 2) large volume H^- ion sources with "spatial uniformity", 3) optimization of the H^- extraction from the source, and 4) high energy acceleration and good beam optics. For these key R&D issues, both plasma and neutrals have to be understood in detail [97, 98].

The volume H^- production (VP) is a two-step process:

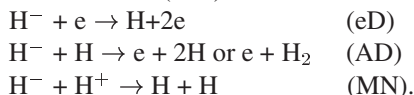
1) vibrational excitation process by fast electrons ($\sim 20\text{--}50\text{eV}$): $e_f + \text{H}_2 \rightarrow e + \text{H}_2(\nu)$ (EV).

2) dissociative attachment process by slow electrons ($\sim 1\text{eV}$): $e_s + \text{H}_2(\nu) \rightarrow \text{H} + \text{H}^-$ (DA).

This basic understanding of the production mechanism leads to the "Tandem Type" concept for a source. For efficient H^- production, the source chamber is divided into two parts with a relatively strong transverse magnetic

field, i.e., the source chamber is divided into the “driver region” and the “extraction region”. In the driver region, fast electrons ($E_e > 20\text{eV}$) are formed, which are very efficient for the first process (EV). They are confined in the multi-cusp magnetic field. In the extraction region, the electron temperature is kept low ($kT_e \lesssim 1\text{eV}$) to enhance the second process (DA). The transverse magnetic field acts a filter field to prevent energetic primary electrons from entering the extraction region.

In addition, the main destruction processes are the electron (eD) and associative (AD) detachment and mutual neutralization (MN):



To enhance the VP, VP sources have to be operated at a relatively high pressure of neutral gas ($\sim 1\text{Pa}$). This high gas pressure inside the source results in a high gas pressure in the extraction gap between the PG and the EG, which in turn causes a significant electron stripping loss (eD) of extracted H^- ions in the extraction channel. To overcome this problem, Cs-seeded surface production (Cs-SP) is generally utilized to obtain an intense H^- ion beam at low pressures ($\lesssim 0.3\text{Pa}$). Significant increase (by a factor of 3-5) in H^- output is obtained with such Cs-seeding at low pressures. The enhancement of H^- ions with Cs seeding is believed to be the results of H^- surface production, because the H^- ion production in the Cs-seeded condition is largely dependent on the work function of the PG surface [99,100]. H^- ions are produced at the cesiated PG surface with a low work function through desorption/backscattering of the incident H atoms and H^+ ions.

4.2 The JAEA arc source

A typical example of the tandem-type source (the JAEA 10 ampere H^- source) is shown in fig.20. The plasma chamber is the same as the JT-60U negative ion source. The dimensions of the plasma chamber are 240mm in width (in the X-direction), 480mm in height (in the Y-direction) and 204mm in depth (in the Z-direction). Four pairs of tungsten filaments are inserted into the plasma chamber from the feed-through at the side walls. To produce the arc-discharge plasma, the plasma chamber wall and the filaments act as anode and cathode, respectively. The plasma chamber wall is surrounded by the multi-cusp magnets to confine the source plasma. A pair of filter magnets is installed to produce the transverse magnetic field and to form the extraction region near the Plasma Grid (PG) surface. Volume produced H^- ions near the PG are extracted from the multi aperture on the PG by the extraction grid (EG).

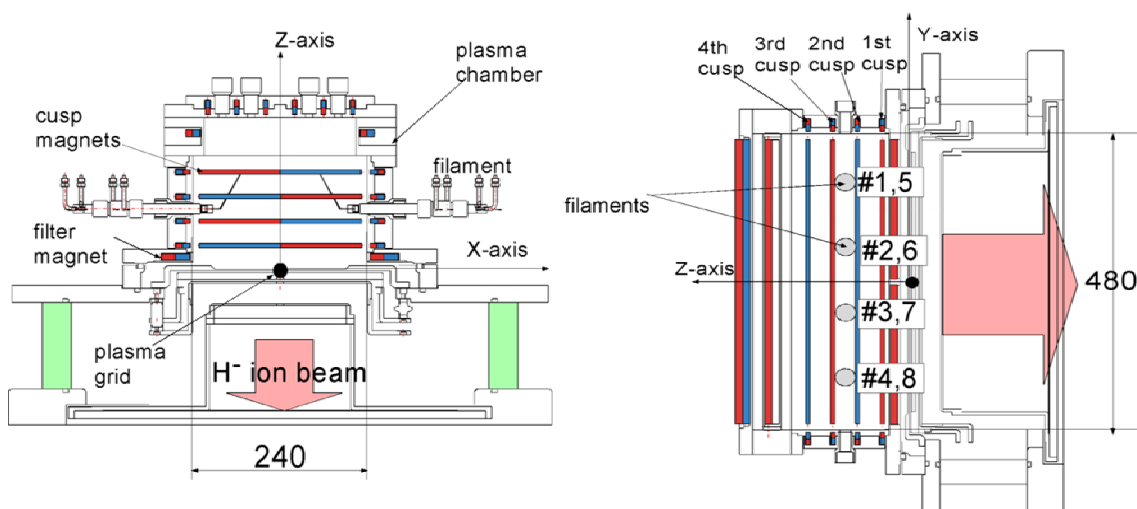


Fig. 20 Schematic diagram of the JAEA 10A negative ion source (from [101]).

In the JAEA 10A source (fig.20), Cs is evaporated from a Cs oven on the back plate to enhance H^- production under the low-pressure condition of $\sim 0.3\text{Pa}$.

4.2.1 Neutral Transport Modeling

Recent experiments in the JAEA 10A H^- source show an interesting feature concerning the non-uniformity of the extracted beam [101, 102]. This H^- beam non-uniformity strongly depends on the dominant production mechanism, i.e., either pure "volume" H^- production (VP) or Cs-seeded "surface" H^- production (Cs-SP). In fig.21a, the measured spatial profiles of H^- beam intensity in the longitudinal direction (the Y-direction in fig.20) are compared between a VP-dominated (without Cs) and SP-dominated (with Cs) case. The beam intensity is significantly reduced for the VP-dominated case, while it is clearly enhanced for the SP-case. Fig.21b shows the electron temperature profile along the vertical direction at the position 14 mm inside from the PG surface. In both the VP and SP cases, T_e profiles are almost the same. At the top side, T_e increases significantly in both cases. The beam non-uniformity in fig.21a strongly correlates with the non-uniformity of T_e in fig.21b. In the VP-dominated case, the destruction of H^- ions in the high- T_e region is the main reason for the beam uniformity. In the SP-dominated case the following two possibilities have been considered: 1) the plasma non-uniformity might affect the surface conditions (e.g. PG surface temperature), and 2) the plasma non-uniformity might produce a local enhancement of neutral atom and/or ion fluxes to the PG surface. In both cases, the resulting local enhancement or reduction of H^- surface production possibly leads to the beam non-uniformity. To examine the first possibility, careful measurements of the PG surface temperature T_{PG} and the work function $f_{W,PG}$ have been done [101]. The results show that T_{PG} and $f_{W,PG}$ are fairly uniform along the vertical direction. This rules out that the first possibility can explain the H^- beam non-uniformity observed in the experiments.

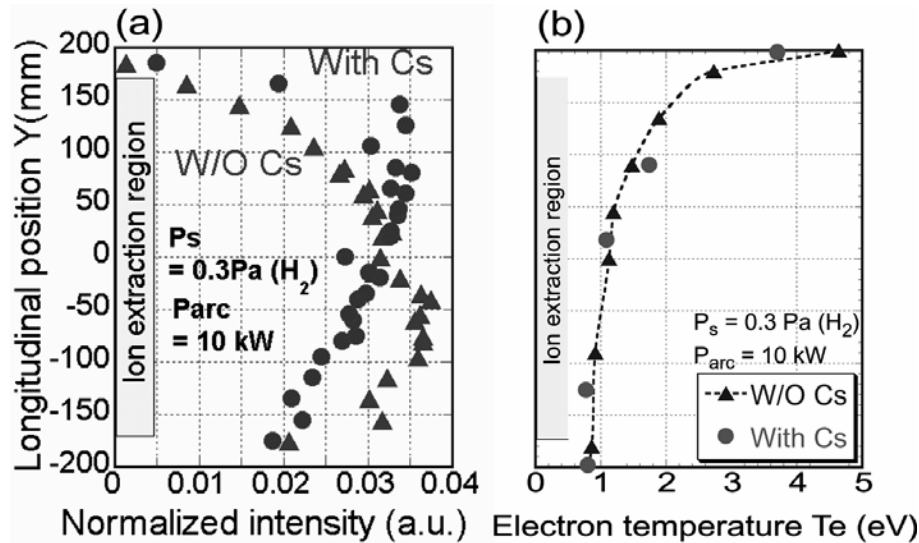


Fig. 21 Spatial profiles of (a) extracted H^- beam intensity and (b) electron temperature in the longitudinal direction measured in the JAEA 10A source. Comparison between the pure volume production (triangle) and the Cs-seeded surface production (circle) (from [101]).

To examine the second possibility, a systematic numerical study on the neutral transport has been done [103–105]. Production and transport processes of H^0 atoms are numerically simulated using a 3D Monte Carlo transport code in the realistic 3D geometry of the JAEA 10A source shown in fig.20. The amount of H^0 atoms produced through dissociation processes of H_2 molecules is calculated from the electron temperature and density obtained by Langmuir probe measurements. The high-energy tail of electrons, which greatly affects the H^0 atom production, is also taken into account by fitting a single-probe characteristic as a two-temperature Maxwellian distribution. The result confirms that the H^0 atom production is locally enhanced in the high-electron-temperature region, where electrons in the high-energy tail are localized as shown in fig.22a. The produced H^0 atoms are traced including the energy relaxation processes of the H^0 atoms, which affect the surface H^- ion production rate. The result shows that the "first-flight H^0 atom flux (FFAF)" of H^0 atoms with high kinetic energies increases near the high-electron-temperature region because of the localization of the H^0 atom production. According to the Rasser's equation [106] for a Cs/W surface, high-energy H^0 atoms have a large surface H^- ion production

rate. Therefore, the surface H^- ion production also increases near the high-electron-temperature region as shown in fig.22a. The uncertainties in the surface models, e.g., the surface H^- production rate, particle and energy reflection coefficient of H atoms from the wall, especially, the reflection coefficient of the Cs/W surface for low energy H atoms, etc, are checked by adopting a different model of H^- production [107] and/or sensitivity studies on these assumptions [105]. As far as the gradient (slope) of the H^- atom production profile is concerned, the results shown in fig.22a are fairly robust and not so much dependent on these assumptions.

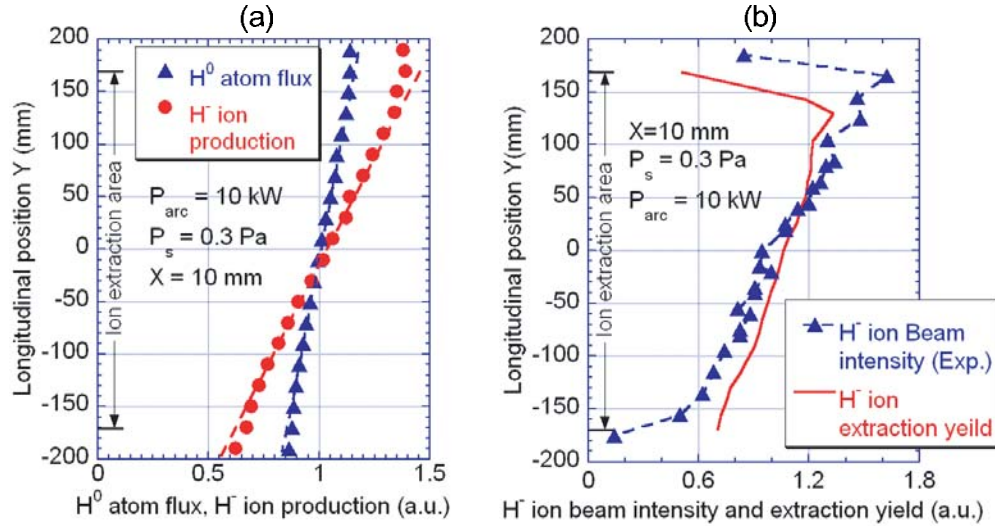


Fig. 22 (a) Normalized longitudinal profiles of the calculated H^0 atom flux on the plasma grid (PG) and the resultant H^- ion production on the PG surface at $X = 10$ mm. (from [105]), (b) Longitudinal profiles of the measured H^- ion beam intensity and calculated H^- ion production on the plasma grid surface at $X = 10$ mm (experimental data from [101]).

4.2.2 H^- Transport Modeling

Based on the H^- production profile obtained from the neutral transport calculation above, the H^- extraction yield is calculated by a 3D H^- transport code [103]. The numerical results of H^- extraction yield are compared with the H^- beam profile in the experiments in fig.22b and a reasonable agreement has been obtained. The local enhancement of the H^0 atom production due to the high electron temperature and the resulting non-uniformity of the H^0 atom flux to the plasma grid (PG) are possible origins of the H^- ion beam non-uniformity observed in the JAEA 10 ampere negative ion source. Based on this, a tent filter concept with the proper setting of filament location was proposed which significantly improved the H^- ion beam uniformity [101, 108].

Differently, following the pioneering NIETZSCHE code [109, 110], various H^- transport codes [111-115] have been developed and successfully applied to explain several phenomena in VP sources and Cs-seeded hybrid sources. The negative ion trajectories are calculated by solving numerically the equation of motion, while the atomic processes of destruction, of elastic collision with background H^+ ions and of charge exchange with H atoms are incorporated by a Monte Carlo method. This allows to calculate the extraction probability of H^- ions produced at any location inside the source for a given background plasma and neutral profiles. Momentum and energy relaxation processes of H^- ions from their birth velocity and energy inside a tandem ion source, i.e., H^- transport process in "velocity space", was analyzed in order to understand the velocity distribution of H^- ions inside the ion source and to explain the good beam optics of extracted H^- ions [113, 115]. The result shows that energy relaxation by Coulomb collisions plays an important role for the H^- temperature in low pressures. Subsequently, the effect of charge exchange collisions of H^- with H has been studied [116, 117] for a relatively high pressure range (0.5 – 1.6 Pa). This plays an important role for the H^- energy relaxation process in these conditions.

4.2.3 PIC Modeling of Extraction Physics

A large enhancement of extracted H^- current was observed in the Camembert III experiments in the presence of a “weak” transverse magnetic field [118]. A pair of magnets installed in the extraction region produces the weak (a few tens of Gauss) stray magnetic field inside the plasma chamber in the small region just in front of the extraction hole (fig.23). This weak magnetic field strongly affects the potential structure and the H^- extraction. A detailed review of the experiments has been recently given in [97]. In order to understand the effect of this weak transverse magnetic field on the potential structure near the extraction aperture and the resultant H^- extraction, Sakurabayashi *et al.* have done a systematic numerical study [119-121] based on the PIC method [86]. The 2D3V PIC modeling shows that the difference in dynamics between electrons and ions in the presence of the “weak” magnetic field leads to a significant change of this potential structure near the PG. This then results in an enhancement of the H^- extraction.

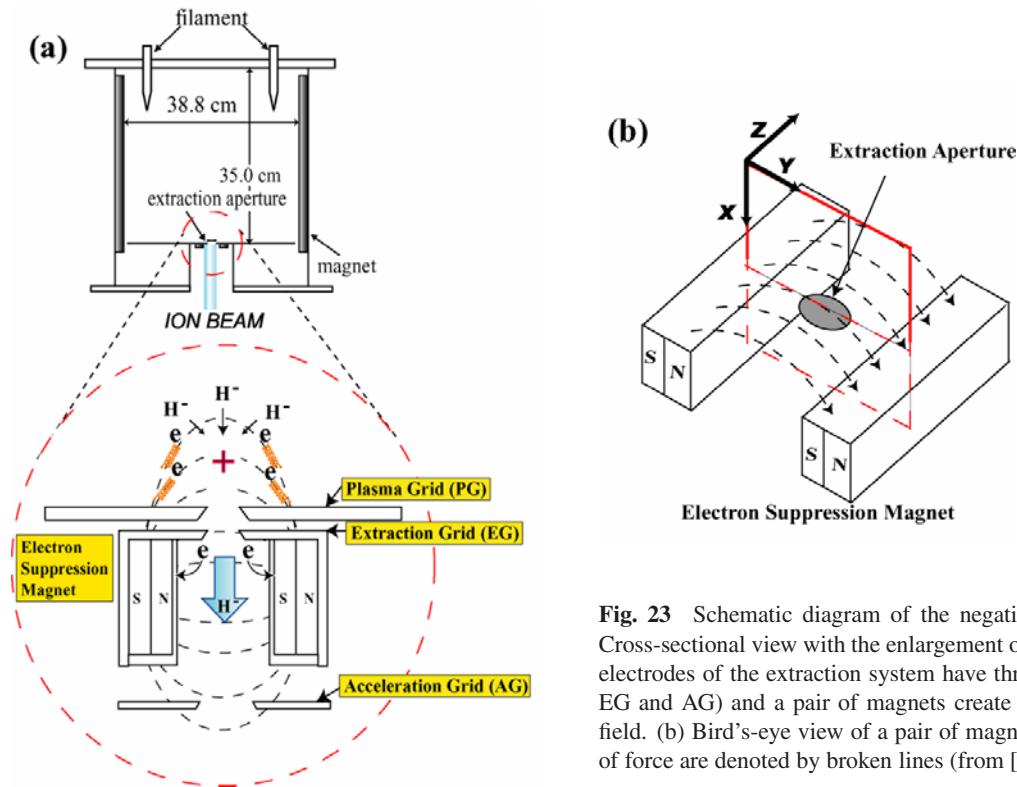


Fig. 23 Schematic diagram of the negative ion source. (a) Cross-sectional view with the enlargement of the extractor. The electrodes of the extraction system have three electrodes, (PG, EG and AG) and a pair of magnets create the weak magnetic field. (b) Bird's-eye view of a pair of magnets. Magnetic lines of force are denoted by broken lines (from [119]).

An improved 2D3V PIC code was developed [122], which is suitable also for the analysis of extraction of surface produced H^- ions. For simplicity (see fig.24), only the region close to the extraction opening has been modeled and a 2D slab geometry has been used. The x -axis is taken to be parallel to the direction of the H^- beam extracted from the aperture, while the y -axis is parallel to the PG. A pair of magnets with an infinite length in the z -direction is installed in the extraction region. The model geometry in fig.23 is assumed to be periodically extended over the y -direction with respect to $y = 0$ and $y = 2L_y$ boundaries. To speed up the calculation, only half of the region ($0 \leq \tilde{y} \leq \tilde{L}_y$) in the y -direction is used as a calculation domain. To do so, a symmetry boundary condition for the potential ($\partial\tilde{\Phi}/\partial\tilde{y} = 0$) is applied. Along the PG surface, $\tilde{\Phi}$ is fixed to be zero ($\tilde{\Phi} = 0$). At the right-hand side boundary ($\tilde{x} = \tilde{L}_x$), $\tilde{\Phi}$ is also fixed to be a given voltage $\tilde{V}_{applied}$, i.e., $\tilde{\Phi}(\tilde{L}_x, \tilde{y}) = \tilde{V}_{applied}$.

At $\tilde{t} = 0$, large numbers of positive and negative charged particles are uniformly loaded in the source region ($0 < \tilde{x} < 10$, $0 < \tilde{y} < 25$). Particles crossing the left boundary ($\tilde{x} = 0$) are reloaded, with a velocity chosen from a half-Maxwellian with a thermal speed determined by the initial temperature kT_{0j} . H^+ ions that strike the PG surface are assumed to be recycled as neutrals and then re-ionized in the source region ($0 < \tilde{x} < 10$, $0 < \tilde{y} < 25$). A pair of H^+ ion and electron is reloaded. The H^+ ion and the electron velocities are chosen, respectively, from a Maxwellian with respective temperatures kT_{0i} and kT_{0e} . On the other hand, electrons and H^- ions which

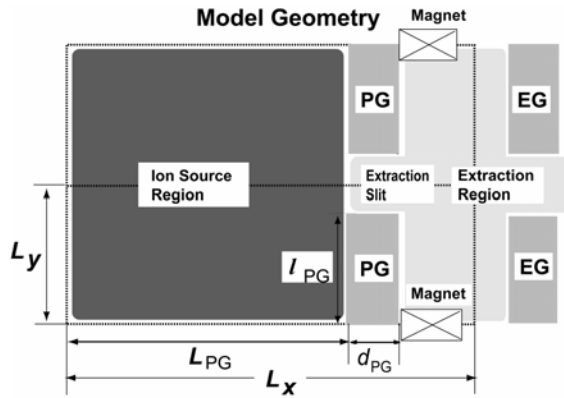


Fig. 24 Model geometry used in the PIC simulations (from [122]).

reach the PG surface are simply removed from the system. Particles crossing the boundary $\tilde{y} = 0$ or $\tilde{y} = \tilde{L}_y$, are reloaded so as to satisfy the symmetric boundary condition with respect to these boundaries. Finally, if particles reach the right-hand-side boundary ($\tilde{x} = \tilde{L}_x$), they are removed from the system.

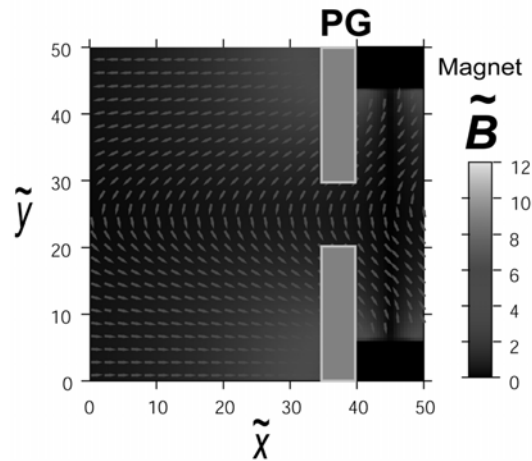
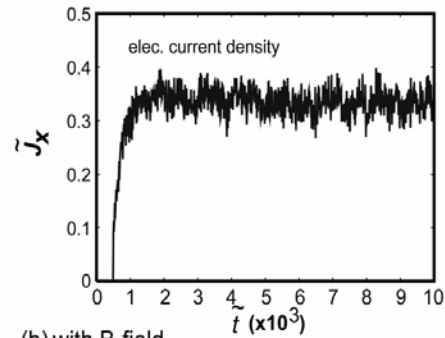


Fig. 25 2D spatial profile of the strength of the normalized magnetic field $|\tilde{\mathbf{B}}| = \sqrt{\tilde{B}_x^2 + \tilde{B}_y^2}$ used in the simulation. The direction of $\tilde{\mathbf{B}}$ at each point is also shown by arrows (from [122]).

The 2D spatial profile of the normalized magnetic field $|\tilde{\mathbf{B}}| = \sqrt{\tilde{B}_x^2 + \tilde{B}_y^2}$ is shown in fig.25. The magnetic field is calculated at each point by using the analytical solution based on the surface magnetic charge model [123]. The magnitude of the surface magnetic charge $\pm\Delta m$ is specified so as to satisfy the following condition: $\tilde{r}_{Le} < \tilde{L}_x$, $\tilde{L}_y \ll \tilde{r}_{LH^+}$, \tilde{r}_{LH^-} where \tilde{r}_{Lj} is the normalized Larmor radius of j -th-species ($\tilde{r}_{Lj} = r_{Lj}/\lambda_{De}$),

(a) without B-field



(b) with B-field

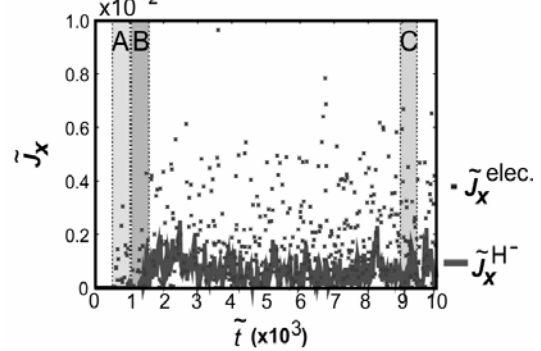


Fig. 26 Time evolution of the space-averaged current density in the extraction channel with $\tilde{V}_{applied} = -25$: (a) without B-field and (b) with B-field (from [122]).

and \tilde{L}_x, \tilde{L}_y are the normalized system length. Thus, electrons are magnetized, while positive and negative ions are not magnetized near the PG.

To understand the effect of the weak magnetic field on H^- extraction, the following two cases are simulated: Case (I) without the magnetic field ($\tilde{\mathbf{B}} = 0$) and Case (II) with the magnetic field $\tilde{\mathbf{B}}$ in fig.26. The remaining calculation conditions are the same in both cases. Initially, the total number of 2×10^5 super particles is loaded in the source region ($0 < \tilde{x} < 10, 0 < \tilde{y} < 25$) and the simulation is started with the applied voltage $\tilde{V}_{applied} = +25$. The ratio of the total number of the H^+ ion, electron and H^- ion is set to be $N_{H^+}^{sp} : N_{elec}^{sp} : N_{H^-}^{sp} = 10 : 9 : 1$.

Fig.26 compares the time evolutions of the extracted current densities, which are the space-averaged values over the extraction channel. In fig.26a [Case (I) without B-field], the electron current dominates the extraction current ($\tilde{J}_x^{elec} \gg \tilde{J}_x^{H^-}$). The extracted H^- current $\tilde{J}_x^{H^-}$ is much smaller. On the other hand, in fig.26b [Case (II) with B-field], the H^- current density $\tilde{J}_x^{H^-}$ becomes relatively large (about two times larger in the time average compared with that in Case (I)), and comparable to \tilde{J}_x^{elec} .

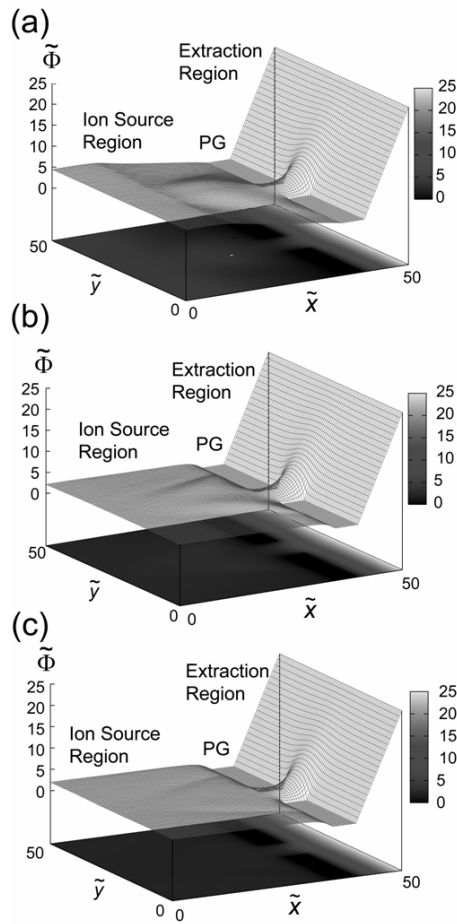


Fig. 27 The 2D spatial profiles of $\tilde{\Phi}(\tilde{x}, \tilde{y})$ with B-field. fig. (a), (b) and (c) are corresponding to the profiles during Phase A, B and C in fig.26b (from [122]).

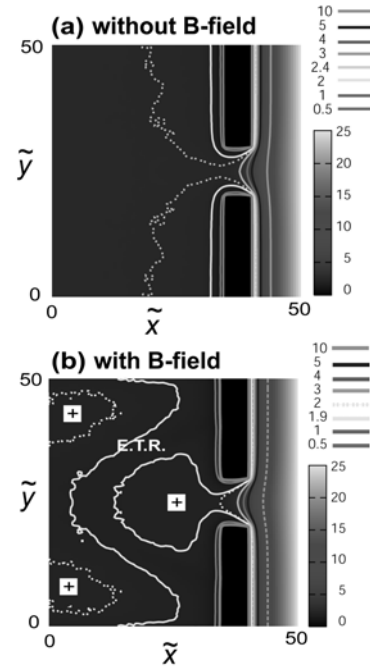


Fig. 28 Contour plots of $\tilde{\Phi}(\tilde{x}, \tilde{y})$ in Phase C in fig.26: (a) without B-field, and (b) case with B-Field. In fig.(b), a mushroom-shaped plateau is seen between the electron trapping region (E.T.R.) and the extraction aperture (from [122]).

The 2D spatial profiles of the electric potential are shown for Case (II) in fig.27. Fig.27a, (b) and (c) correspond to the profiles at different time, Phase A, B and C. To remove the fast time-scale fluctuations of $\tilde{\Phi}(\tilde{x}, \tilde{y})$, the potential is time-averaged over each phase. As seen from fig.28a, a potential peak can be seen at the initial phase

in front of the extraction slit due to the trapping of electrons by the “weak” magnetic field. On the other hand, the H^+ and H^- ions are not magnetized. Therefore, H^- ions are collected by the positive potential peak and move together with H^+ ions towards the PG to ensure the plasma neutrality. Then, the peak potential decreases during Phase B.

The contour plots of the potential during the quasi-steady state (Phase C) are compared in fig.28 between Case (I) and Case (II). The weak magnetic field in Case (II) produces a significant modification of the potential structure in front of the extraction slit. A relatively large-scaled and mushroom-shaped plateau is formed for Case (II) with a B-field between the electron trapping region and the extraction aperture.

In addition to the effect of weak magnetic field, the surface H^- production affects the potential structure near the PG and by this the resultant H^- extraction. After the system reached a quasi-steady state with pure volumetric processes, H^- injection has been started from the PG surface with a constant source rate (10 particles per time step). The initial positions of the surface produced H^- ions are randomly chosen and almost uniformly distributed in the \tilde{y} direction on the PG surface (at $\tilde{x} = 35$). The initial velocities are simply chosen from a half-Maxwellian distribution with $T_{H^-} = 0.25\text{eV}$. The surface-produced H^- ions crossing the left boundary ($\tilde{x} = 0$) are assumed to be destructed and removed from the system. All other conditions are the same as before.

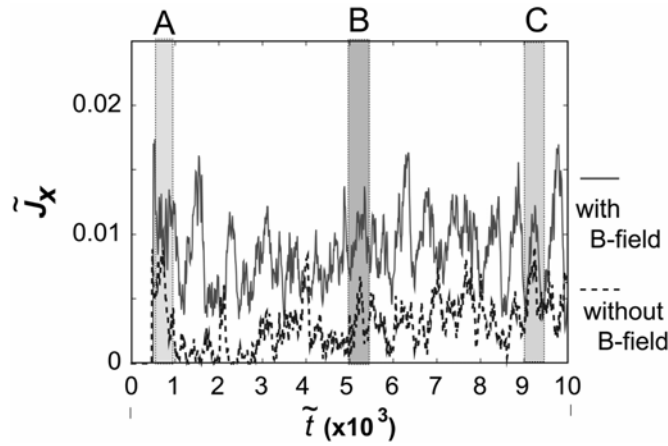


Fig. 29 Time evolutions of the extracted H^- current density $\tilde{j}_x^{H^-}$ with surface H^- production (broken line: without B-field, solid line: with B-field) (from [122]).

Fig.29 shows the time evolutions of the extracted H^- current density $\tilde{j}_x^{H^-}$. The broken line is the result for the case without B-field [Case (III)], while the solid line is for the case with B-field [Case(IV)]. Even with the strong surface H^- production, the weak magnetic field effectively enhances the H^- extraction.

In both cases, initially, the number of H^- ions in the system increases due to strong surface H^- production, while the number of electrons decreases. As times goes on, they almost reach a quasi-steady state value. The potential structure inside the source self-organizes and the number of particles for each species in the system reach a new quasi-steady state in the case with the surface H^- production.

The 2D spatial potential profile for Case (IV) with B-field during Phase A, B and C are shown in fig.30a, (b) and (c), respectively. To understand the effects of surface production on the potential structure, it is interesting to compare these results with those in fig.28, i.e., without the surface H^- production. The most distinct feature with the surface H^- production is the formation of a double sheath structure just in front of the PG surface, i.e., a negative potential region is produced due to the strong surface H^- production. In addition, the plasma potential inside the source is reduced, i.e., $\tilde{\Phi}(\tilde{x}, \tilde{y}) \approx 0.8 - 1$ for Case (IV) with the surface H^- production while $\tilde{\Phi}(\tilde{x}, \tilde{y}) \approx 2$ for Case (II) without surface H^- production in Phase C.

To see the effect of the weak magnetic field on the potential structure with the surface H^- production, the contour plots of the potential between the Case (III) without B-field and the Case (IV) with B-field are compared in fig.31. A significant change in the potential structure is seen for the Case (IV) with the B-field. A relatively large scale, positive potential plateau is formed in front of the extraction aperture as in fig.29. The “weak” transverse magnetic field is shown to be effective also with the surface H^- production.

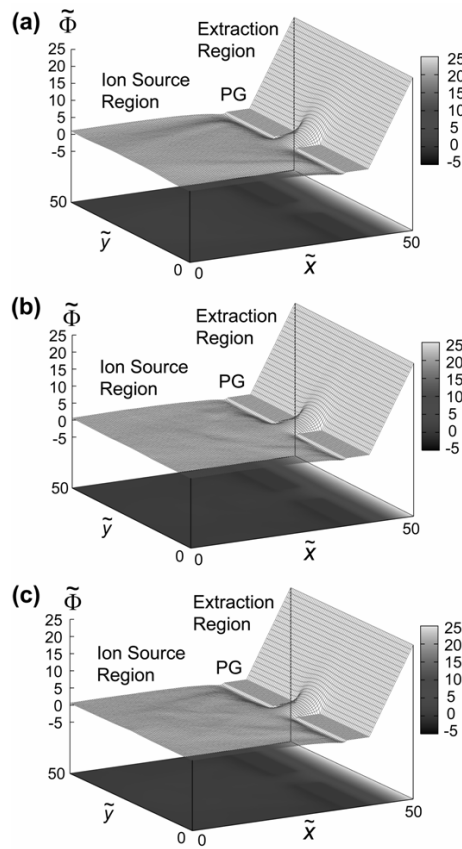


Fig. 30 2D spatial profiles of $\tilde{\Phi}(\tilde{x}, \tilde{y})$ with both the surface H^- production and B-field. Fig. (a), (b) and (c) are corresponding to the profiles in Phase A, B and C in fig.29 (from [122]).

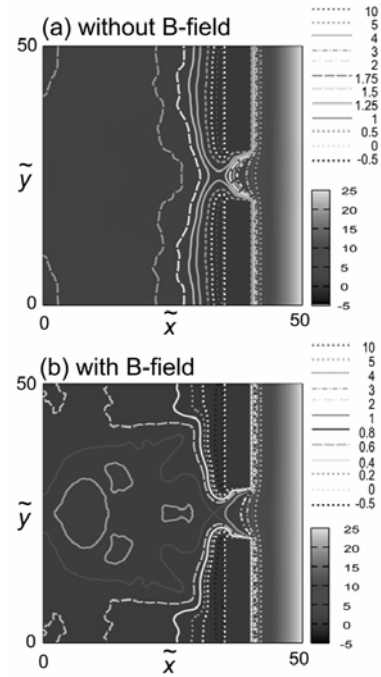


Fig. 31 Contour plots $\tilde{\Phi}(\tilde{x}, \tilde{y})$ in Phase C in fig.29 with surface H^- production: (a) without B-field, and (b) with B-field (from [122]).

4.3 Radio frequency inductively coupled negative ion source

The negative ion source for ITER has been officially chosen to be the radio frequency inductively coupled discharge developed at Max-Planck Institute für Plasmaphysik in Garching [124] (see fig.32a).

This source consists of three parts: the cylindrical driver, where the RF coils are coupled to the H_2 gas to generate the plasma, the rectangular expansion region, where the plasma expands into the actual source body, and the extraction region. The latter two are separated by a non homogeneous magnetic field parallel to the plasma grid of the order of 5-7 mT, the filter field (red line in fig.32a). In fact, as mention in the paragraph 4.1, it is generally accepted that most H^- ions are produced in the volume by a two-step process which involves dissociative attachment of slow electrons ($T_e < 2$ eV) to highly vibrationally excited levels of hydrogen molecules H_2 (optimum vibrational level $v=4-9$ reached at $T_e > 10$ eV) [125]. For this reason, the optimum condition for H^- formation is not compatible with that for $H_2^+(v)$ production and a magnetic filter has been introduced to separate the negative ion source into two regions where the electron temperature is optimized for each the two processes. The cooling-down from the expansion region is further assisted by magnets in the extraction electrode which are primarily there to deflect the co-extracted electrons (blue line in fig.32b). The driver is mounted on the back of the source body and consists of a 245mm id alumina cylinder with a water-cooled RF coil connected to a 1MHz oscillator. An internal edge cooled copper Faraday screen protects the alumina cylinder from the plasma. In order to reduce the sputtering by the plasma, the plasma side of Faraday screen is covered by a thin tungsten layer. Due to the Faraday screen that allows only inductive coupling, a so-called starter filament is necessary in order to ignite the plasma.

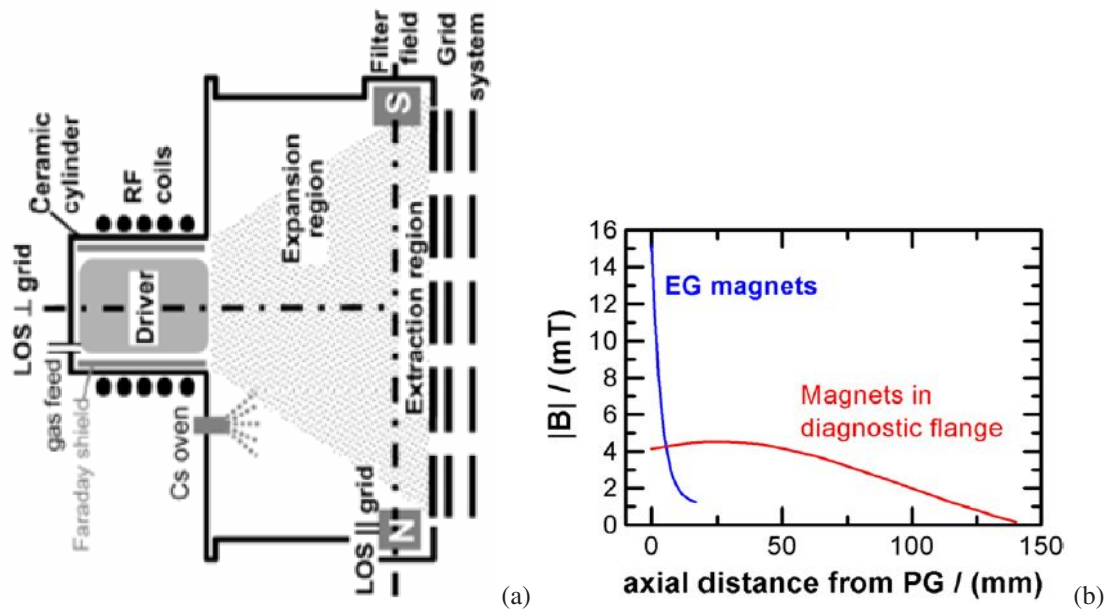


Fig. 32 (a) Scheme of the radio frequency inductively coupled negative ion source developed at Max-Planck IPP in Garching and (b) Magnetic field as a function of the axial distance from the plasma grid created by the electron deflection magnets inserted into the extraction grid (blue line) and by the magnetic filter (red line).

In addition to volume production of negative ions, the extraction current density of negative ions is strongly increased by adding Caesium and generating a lot of additional negative ions from the caesiated surfaces. Caesium is delivered from an oven connected to the back flange of the source body. The nozzle of the oven penetrates a few millimetres into the plasma. Caesium is dispensed at a rate of typically 10 mg h^{-1} .

The separation of this negative ion source in two regions allows the development of two different un-coupled simulations, described in paragraphs 4.3.1 and 4.3.2, respectively.

All the relevant parameters are listed in Table 2.

Table 2 Operative parameters of the radio frequency inductively coupled negative ion source @ Garching.

Driver region: $L_z \times R$	0.2 x 0.12 m
Expansion region: $L_z \times L_x \times L_y$	0.2 x 0.3 x 0.6 m
Input Power	170 kW
Current coil	100 A
Frequency	1 MHz
Pressure	0.3 Pa
Extraction grid potential: PG/EG/AG	-20 kV/-14 kV/0 V

4.3.1 Gas kinetics and dynamics in the expansion region

In order to better understand the formation and destruction of high vibrational levels of hydrogen molecules in the expansion region, a Direct Simulation Monte Carlo (DSMC) model (from the exit plane of the driver to the magnetic filter location) has been performed [126]. We consider 16 species of neutral particles [$\text{H}(n=1s)$ and $\text{H}_2(v=0, \dots, 14)$]. The particle representation allows the self-consistent inclusion of the gas-surface interaction, a very important issue in the vibrational population distribution. Furthermore, it includes also rarefied gas effects, important at low pressures (0.3 Pa).

This is a neutral dynamics module preparing and describing the physics in the transition zone between the source and extraction region. This model is only valid for conditions, where a separation of the neutral from plasma dynamics is possible. For hydrogen gas this is usually a good approximation for electron temperatures

greater than 5 eV.

4.3.1.1 Bulk module

In the expansion region, the plasma is continuously replenished from the driver region. Therefore, the plasma subsystem is considered as a fixed background. An axial decay due to plasma expansion is implemented using the following fitting formula from the experimental measurements of electron density and temperature [127]:

$$n_e(z) = n_{e,0} e^{-z/0.13} \quad (5)$$

$$T_e(z) = T_{e,0} e^{-z/0.23} \quad (6)$$

where z is in meter and $n_{e,0}=1 \times 10^{18} \text{ m}^{-3}$, $T_{e,0}=8 \text{ eV}$ are the values at the driver exit plane. The molar fractions of the ion species H_x^+ is estimated for the operative conditions typical in the radio frequency negative ion source, as follows:

$$\chi(H^+) = 0.25; \chi(H_2^+) = 0.34; \chi(H_3^+) = 0.41 \quad (7)$$

while the ion temperature is fixed at $T_i=1 \text{ eV}$.

Through this plasma background, neutral pseudo-particles of H and H_2 are launched from the source line (driver exit plane, $z=0 \text{ m}$ in fig.32a) with an half-Maxwellian velocity distribution and with a Boltzmann vibrational population for a fixed temperature (translational temperature $T_{transl}=1200 \text{ K}$ equal to the vibrational temperature T_{vib} [128, 129]):

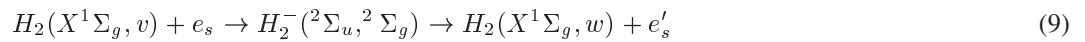
$$n_{H2(v)} = n_{H2} \left(1 - e^{-\varepsilon_v/kT_{vib}}\right) e^{-\varepsilon_v/kT_{vib}}, \quad (8)$$

where $n_{H2}=P/kT_{transl}$ is the total density of molecular hydrogen and ε_v is the energy of the vibrational level v calculated using the Morse anharmonic oscillator. A ratio of $n_H/n_{H2}=0.2$ [128, 129] between atomic and molecular density is defined at the source. An open boundary condition is implemented on the right side of the simulation domain (particles crossing this line are deleted from the list).

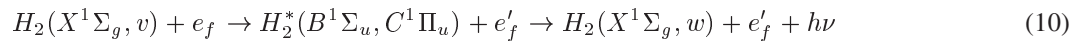
The first electronic state of H ($n=1s$) is considered. Due to the typical neutral time scale ($\Delta t \approx 10^{-8} \text{ s}$), the spontaneous emission process is considered fast and all electronic excited states of H decay into the ground state. For the molecules, the fifteen vibrational levels of the fundamental electronic state of H_2 ($X^1 \Sigma_g^+$, $v=0, \dots, 14$) are taken into account. Due to the high ionization coefficient ($\alpha > 10^{-2}$) and to the electron temperature involved, the rotational levels have already attained equilibrium [130]. Indeed, the rotational relaxation is much faster than vibrational relaxation $\tau_{eR} \ll \tau_{eV}$ and the assumption of equilibrium between rotational and electron energy modes is acceptable. The same argument is valid between heavy particles (neutral-neutral relaxation). In fact, owing to the scaling of relaxation times $\tau_{VT} \gg \tau_{RT} \sim \tau_{TT}$, one can usually treat the problem of vibrational relaxation by assuming that both the rotational and translational degrees of freedom have already attained equilibrium.

Finally, some molecular electronic states without vibrational structure ($B^1 \Sigma_u^+$, $C^1 \Pi_u$, $D^1 \Pi_u^+$, $B^1 \Sigma_u^+$, $D^1 \Pi_u^+$, $BU\Sigma$, $a^3 \Sigma_g^+$) are also considered as reservoir (they are created in collisions but not destroyed). A complete description requires the inclusion of a collisional radiative model for the electronic excited states. In particular we neglect the coupling between the $a^3 \Sigma_g^+$ state and the $c^3 \Pi_u$ one, which could result in an indirect dissociation of $a^3 \Sigma_g^+$ state.

In the plasma conditions studied here, direct electron-impact excitation appears to be the dominant vibrational heating mechanism. Electron excitation processes include vibrational excitation by low energy electrons acting through the intermediary of the unstable negative ion H_2^- resonances (eV processes):



and vibrational excitation caused by the radiative decay of higher singlet electronic states excited by energetic electrons (eV processes):



The firsts involve excitations with jump $|w - v| < 5$, while the latest are not limited in the vibrational excitation gap. The database reported in [131, 132] has been extended by the eV cross sections for transitions involving $w > 7$, and the full matrix of eV cross sections is now available extrapolating the available data. These electron-molecule cross sections are based on the impact parameter method and the Gryzinski semiclassical approximation. The accuracy of these cross sections is within a factor 2 with respect to experimental data and/or more reliable quantum mechanical calculations. This discrepancy is in any case acceptable in the present model. Proton induced excitation (pV), charge exchange (p-CX) and dissociation (pV-diss) are also included using recent v -selective cross sections [133-137].

Concerning the destruction processes of vibrational states, electronic excitations, ionization, dissociation and dissociative ionization and attachment are all included in the model. In particular, 6 singlet state excitations and 1 triplet state excitation, 10 dissociative channels and 2 dissociative ionizations are considered (see Table 3 for details). A Monte Carlo Collision (MCC) method is used [141].

Table 3 List of the most significant volume processes included in the model.

Reaction	Process	Ref.
1) atom elastic collision	$e + H \rightarrow e + H$	[131,132]
2) atom ionization	$e + H \rightarrow 2e + H^+$	[131,132]
3) vibrational excitation : eV	$e + H_2(v) \leftrightarrow e + H_2(w)$	[131,132]
4) vibrational excitation: EV (via: $B^1\Sigma_u^+, C^1\Pi_u$)	$e + H_2(v) \rightarrow e + H_2(w) + h\nu$	[131,132]
5) electronic excitation: eE (via: $B^1\Sigma_u^+, C^1\Pi_u, D^1\Pi_u^+, B^1\Sigma_u^+, D^1\Pi_u^+, BU\Sigma, a^3\Sigma_g^+$)	$e + H_2(v) \rightarrow e + H_2^+$	[131,132]
6) molecular ionization: eI	$e + H_2(v) \rightarrow 2e + H_2^+$	[131,132]
7) dissociation: eD (via: $B^1\Sigma_u^+, C^1\Pi_u, D^1\Pi_u^+, B^1\Sigma_u^+, D^1\Pi_u^+, BU\Sigma, e^3\Sigma_g^+, c^3\Pi_u, b^3\Sigma_u$)	$e + H_2(v) \rightarrow H + H$	[131,132]
8) dissociative ionization: eDI (via: $X^2\Sigma_g^+, ^2\Sigma_u$)	$e + H_2(v) \rightarrow 2e + H + H^+$	[131,132]
9) dissociative attachment: DA	$e + H_2(v) \rightarrow H + H^-$	[131,132]
10) charge exchange	$H^+ + H \rightarrow H + H^+$	[138]
11) proton excitation: pV	$H^+ + H_2(v) \leftrightarrow H^+ + H_2(w)$	[133,134]
12) proton exchange: p-CX	$H^+ + H_2(v) \rightarrow H + H_2^+$	[135,136]
13) proton impact dissociation: pV-diss	$H^+ + H_2(v) \rightarrow H^+ + H + H$	[137]
14) vibrational-translational relaxation: Vt	$H_2(v) + H \leftrightarrow H_2(w) + H$	[139]
15) vibrational-translational dissociation: Vt-diss	$H_2(v) + H \rightarrow H + H + H$	[139]
16) vibrational-translational relaxation: VT	$H_2(v) + H_2(w) \rightarrow H_2(v \pm 1) + H_2(w)$	[140]
17) vibrational-translational dissociation: VT-diss	$H_2(14) + H_2(w) \rightarrow H + H + H_2(w)$	[140]

Finally, among all the neutral-neutral relaxation processes, the vibrational-translational exchange between molecule-atom (Vt) and molecule-molecule (VT) are investigated. These events are important at high vibrational levels. Concerning Vt, this is due to the high probability to form the intermediate H_3 complex, while as regard VT, this is due to the anharmonicity, and in particular to the reduction of transition energy with an increase of vibrational quantum number [eq. (9),(10)]. In fact, the VT relaxation probability for one-quantum processes $v+1 \rightarrow v$ [142, 143]:

$$P_{v+1,v}^{VT} = P_{1,0}^{VT} \frac{(v+1)}{(1 - \chi_e v)} e^{\delta_{VT} v} \quad (11)$$

has a strong exponential dependence from the vibrational level. This kind of collision is processed using a Direct Simulation Monte Carlo (DSMC) methodology [141]. In our model, a set of cross sections [139, 140] is used allowing multi-quanta transition for Vt and mono-quanta transition for VT. Vibrational-vibrational exchange is neglected due to the low pressure regime.

4.3.1.2 Boundary module

In the model the transverse coordinates x and y of particles are updated and when a neutral collides with the wall (we use copper as wall material), molecular relaxation/dissociation and atom recombination are respectively processed for molecules and atoms.

Concerning H_2 , a constant value of the sticking probability is used [144] ($\gamma_{stick}=0.5$). In the case of reflection, a dissociation probability of $\gamma_{diss}=0.08$ [145] is expected. If the molecule does not dissociate, a set of repopulation probabilities (see fig. 1 in Ref. [146]) is used to choose the final vibrational state after wall collision.

For the case of H impacting on the wall, a more complex situation exists. Again, a constant value of the sticking probability is used (the same used for H_2). If the atom does not stick on the surface the most important non-reactive process (reflection, exchange with the adsorbate and collision induced desorption) is reflection. A fitted formula for the reflection coefficients R_N and R_E is used [147]. If the particle is not reflected, the reactive processes occurring can be classified in three different mechanisms:

1) the *Eley-Rideal* (ER) mechanism, when an atom from the gas phase recombine directly with an adsorbed atom. Quantum mechanical calculations [144, 146, 148] gives a cross section for this reaction as $\sigma_{ER}=0.5 \text{ \AA}^2$.

2) the *hot atom* (HA) mechanism, which consider the interaction of translationally hot hydrogen atoms with the surface. They are temporarily adsorbed and trapped at the surface by means of the mediation of adsorbate or corrugation, propagate on the surface until a pre-adsorbed atom is reached and recombine. This reaction is very important due to the high cross section ($\sigma_{HA}=18 \text{ \AA}^2$) evaluated from quantum mechanical simulation [144, 146, 148]. Moreover, due to the high energy involved in this recombination reaction, the molecules are delivered in excited states (up to $v=9$ as experimentally deduced [149,150]).

3) the *Langmuir-Hinshelwood* (LH) mechanism, when two adsorbate atoms recombine. This process has a minor relevance (2%) due to the low cross section and low vibrational states produced.

The vibrational distribution of the emitted molecule (AV process) is a complex function of incident energy and angle, impact parameter, vibrational state of the adsorbed atom and surface temperature. For simplicity, tabulated values depending only on the impact energy are used (see fig. 3 in Ref. [145]).

Finally, it is well known that at least for low gas pressure, the surface Auger neutralization of H_2^+ (sV_2) and H_3^+ (sV_3) can compete favorably with EV and AV processes and thus provide an additional source of vibrational excitation [151]. A fixed flux of $H_2^+(v)$ distributed following Ref. [151] (see figures 5-8 and 11 there) is generated from the wall:

$$\phi_{H2} = \frac{1}{4} n_i v_{th,i} \gamma_{sV,i} \quad (12)$$

where the index i refers to the ions ($i=2$ for H_2^+ and $i=3$ for H_3^+), $v_{th,i}$ is the ion thermal velocity and $\gamma_{sV,i}=0.6$ is the fraction of incident ions that survives as H_2 after the wall collision. The remaining 40% of the H_2^+ neutralization proceeds through the dissociative channel, $H+H$ ($sA,2$) [151]. The same formula is also applied to H^+ neutralization on the wall $sA,1$, with a neutralization coefficient $\gamma_{sA,1}=0.9$ [152]. The values of the wall neutralization coefficients are very important in relation to the neutral translational temperature. In fact, in these case atoms and molecules are emitted specularly from the wall with the ion temperature. In Table 4 all the simulation parameters are listed.

Table 4 Simulation parameters used into the expansion region model.

Sticking coefficient	$\gamma_{stick}=0.5$	[144]
Reflection coefficients	R_n, R_e (fit)	[147]
Dissociation coefficient	$\gamma_{diss}=0.08$	[145]
Auger neutralization coefficient	$\gamma_{sV,i}=0.6$	[151]
Ion neutralization coefficient	$\gamma_{sA,1}=0.9$	[152]
Dissociative neutralization coefficient	$\gamma_{sA,2}=0.4$	[151]

4.3.1.3 Results

Even if the number of molecules injected from the driver is 5 times larger than atoms, at the end of the expansion region the number of atoms reaches a value of 1.4 times the number of molecules. This is due to the strong electron and surface dissociation and H^+ wall neutralization.

Fig.33 shows the total population of the vibrational states VDF of molecular hydrogen in the electronic ground state at the end of the expansion region ($z \approx 20$ cm). A strong super-thermal non-Boltzmann distribution with a very long plateau is formed extending up to $v=11$. The Boltzmann character is restricted to the first two vibrational levels and it is due the competition between eV, AV and wall relaxation processes. Furthermore, due to the high ionization factor (and in particular to the high density of H_2^+ and H_3^+ ions) and high surface to volume ratio of the expansion chamber, the sV processes play an important role increasing the density of high vibrational levels by one order of magnitude. Less important are the contributions of AV excitation. Finally, the effect of Vt and VT relaxations get more important at very high vibrational levels, while the first levels are substantially unchanged.

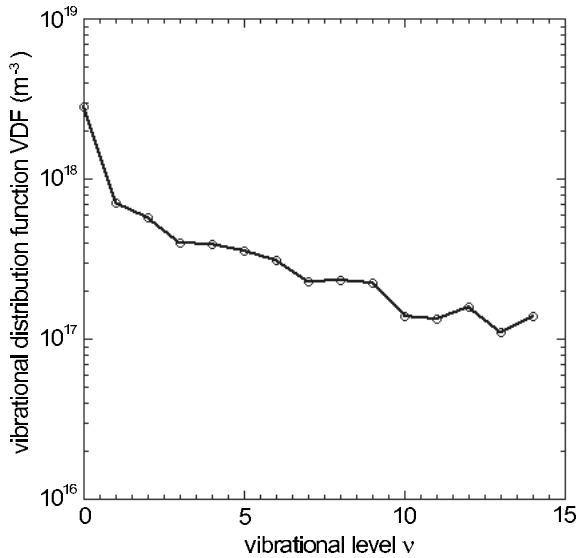


Fig. 33 Total density of vibrational states at the exit of the expansion region ($z \approx 20$ cm); all formation and destruction processes are included.

In fig.34a the axial profile of the vibrational temperatures is shown. In fact, the vibrational distribution function can be characterized by a vibrational temperatures $T_{vib,0-1}$, which provides a measure of the degree of vibrational excitation in low vibrational levels and $T_{vib,0-7}$, which indicates the position of the VDF plateau.

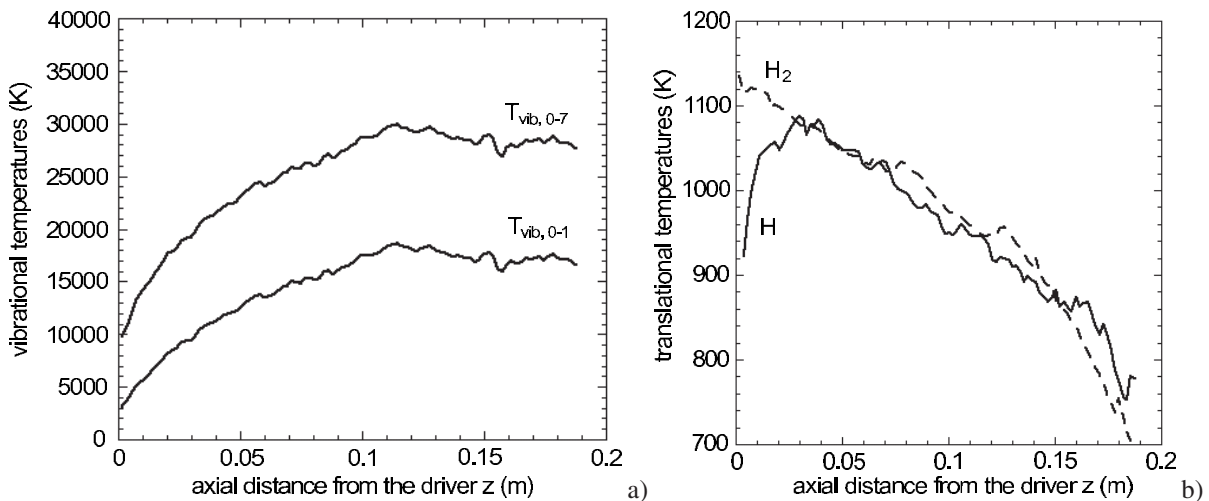


Fig. 34 (a) Axial profile of the vibrational $T_{vib,0-1}$, $T_{vib,0-7}$ and (b) translational H and H_2 temperatures.

They are defined as:

$$T_{vib,0-v} = \frac{E_v - E_0}{k_B \ln \left[1 + \frac{E_v - E_0}{\bar{E}_{vib}} \right]} \quad (13)$$

where the average vibrational energy is $\bar{E}_{vib} = \frac{\sum_v (E_v - E_0) n_v}{\sum_v n_v}$. The vibrational temperature $T_{vib,0-1}$, comprised between 3000 K and 15000 K, is relatively low compared with the electron temperature (about 5 eV) due to the strong wall relaxation effects. This result is consistent with the experiments in Ref. [136] in which the vibrational temperature is lower than 5000 K with an electron temperature of 3 eV and it is in good agreement with the experimental measurements reported in Ref. [129]. Concerning translational temperatures, a cooling down to 700 K due to expansion is experienced.

4.3.2 Plasma-gas coupling in the extraction region

This second part of the work represents the continuation of the previous one (paragraph 4.2), where the neutral population was prepared into the expansion region to allow the negative ion production in the subsequent extraction region. In order to obtain negative ion beams with higher efficiency, it is essential not only create but also understand the fundamental transport mechanism of negative ions produced. Plasma parameters in the region next to the plasma grid PG are considered influential to the amount of extractable H^- current from an ion source. In this region, gradients due to plasma sheath and the presence of a magnetic filter create forces strongly affecting the free flight and collisional events. In fact, experiments [153, 154] have shown that PG bias and magnetic filter have an important role for the enhancement of H^- production (through the electron temperature and density) and extraction. The spatial structure of plasma parameters near the PG is a key point in the transport of negative ions. Parallel magnetic field and strong surface production in cesiated sources can create a complete reversed sheath in front of PG [155]. Furthermore, surface processes through direct surface conversion and/or surface molecular excitation represent important mechanisms for the production of negative ions.

On the basis of these introductory features it is important to have a self-consistent model of the extraction region. The coupling of the vibrational kinetics of H_2 and the plasma dynamics is very important in the region far from the driver where both the electron density and temperature drop down. Therefore, we are using for this region such a coupled model. Differently from the treatment done in the expansion region, where the plasma subsystem was considered a fixed background, in the extraction region charged and neutral particles dynamics are numerically solved in different modules and coupled explicitly. This guarantees an accurate steady-state representation of the system. We are not interested in the temporal evolution of the system.

The simulation domain extends 4 cm from the PG. In fact, as already demonstrated from Monte Carlo calculation [110], the probability for an H^- to reach the grid goes down to zero for distance larger than 3 cm. Two different axial lines are simulated (see fig.34): line A which ends on the extraction hole (open boundary condition) and line B which ends on the cesiated Molybdenum PG surface (fixed potential).

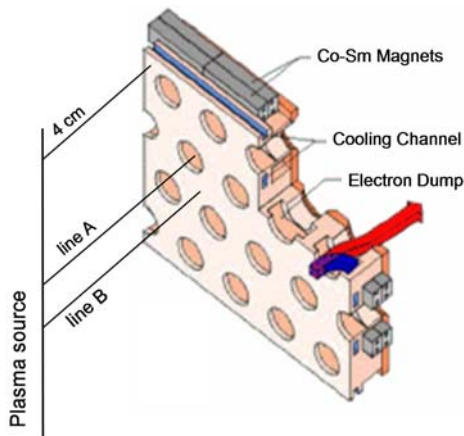


Fig. 35 Schematic diagram of the simulation model. (Online colour: www.cpp-journal.org).

4.3.2.1 Plasma module

The complete motion of electrons and ions (H^+ , H_2^+ and H^- are simulated) is calculated in the self-consistent electric and applied magnetic fields (the profile of B reported in fig.32b is used) by solving the equation of motion, including collisional effects via different Monte Carlo techniques, and using a spatial grid (cell size of the order of Debye length) for the potential calculation, as in a typical PIC cycle. The time step is set equal to the inverse plasma frequency.

The simulation starts with a uniform distribution of maxwellian plasma $n_p=10^{17} \text{ m}^{-3}$ with the same ratio of charged particles present in the expansion region (eq. (4.2)). The following temperatures $T_e=4 \text{ eV}$ and $T_i=1 \text{ eV}$ coming from experimental measurements [156] are used. In order to reproduce the plasma flow detected by measurements using a Mach probe [156], an axial drift component is added to the thermal one: $v_{z,drift}=0.3 \text{ Mach}$. The refluxing methodology is applied (when a particle leaves the domain crossing the left-hand line, it is re-injected into the domain with bulk temperatures). We call this boundary the plasma line (PL) and a Neumann boundary conditions for the Poisson equation is used: $\partial\phi/\partial z|_{PL}=0$.

For charged-neutral particle collisions (reported in table 4.2) the null collision method [18] is used, which ensures high accuracy and high speed of the calculations, while for charged-charged particle collisions (electron detachment, mutual neutralization, etc.) a Direct Simulation Monte Carlo technique [141] is used. Within the PIC module, only charged particles are moved and the code does not follow the dynamic of the neutrals but rather treats the latter as a fixed background with density and velocities profiles from the previous iteration of the neutral module. When ions reach the PG surface, among the different processes occurring (reflection, neutralization, recombination, dissociation, etc.), the activation of high vibrational states (the same used in the expansion region, paragraph 2.2) and the formation of negative ions by electron capture from the wall are the most important, because they are directly related to the negative ion production. The H^- yield can be expressed as a function of incident energy E_{in} by the formula [107]:

$$Y(E_{in}) = R_N \eta_0 \left(1 - \frac{E_{th}/R_E}{E_{in}} \right), \quad E_{in} \geq E_{th}/R_E \quad (14)$$

where R_N and R_E are the particle and energy reflection coefficients, respectively, while η_0 is the height and E_{th} is the threshold energy for the electron transfer probability. This scheme reflects the two-steps idealization of this mechanism: the backscattering as neutral atom and the electron transfer. H^- are launched from the surface with energy of $R_E E_{in}$ and with a cosine angular distribution. The value of the parameters used for a caesiated Molybdenum surface are reported in table 5.

4.3.2.2 Neutral module

The neutral module proceeds that developed for the expansion region. Every 1000 PIC cycles (in order to allow the ion system to relax), the neutral module is called. Neutral pseudo-particles are launched from the source line with a half Maxwellian velocity distribution: $T_{transl}=700 \text{ K}$ (see fig.34b). The VDF reported in fig.33 is used to select the vibrational level of molecules injected from the plasma line. A ratio of 1.4 between atomic and molecular density is kept at the source. Different weights (two order of magnitude larger than used in the PIC module for the charged particles), cell sizes (of the order of neutral mean free path) and time steps are used in the neutral module.

All the collisions involving neutral-plasma are processed using values of plasma densities and velocities averaged on the previous PIC module. The most important mechanism added in the neutral module is the negative ion production from the caesiated PG by neutral impact. Two types of ion emission are considered: thermodynamic and non-thermodynamic equilibrium surface ionization [157, 158]. In the first case, atoms impinging on the metal surface may be emitted as atoms or ions in subsequent evaporation processes after mean residence times long enough for the establishment of equilibrium. In this case, the probability of leaving the surface as a negative ion is given by the Langmuir-Saha relation:

$$Y = \left[1 + \frac{g_0}{g_-} e^{(\phi - E_A)/kT_H} \right]^{-1} \quad (15)$$

where E_A is the electron affinity of H , Φ is the work function of the caesiated Mo surface, g_0 and g_- are the degeneracy of atom and negative ion respectively. The second mechanism, called hot atom, is the result of the

interaction of a fast particle with the surface and eq. (3) is used. The value used for these parameters are reported in table 5.

Table 5 Simulation parameters used for the surface negative ion production [107].

Parameters	Ions (H^+ , H_2^+) per nucleus	Neutrals (H , H_2) per nucleus
$R_N \eta_0$ (eq. (14))	0.30	0.42
E_{th}/R_E (eq. (14))	2.0 eV	1.05 eV
ϕ (eq. (15))	/	1.5 eV
E_A (eq. (15))	/	0.75 eV

When the neutral subsystem reaches a steady state, the plasma module is called again with the latest neutral results. This iteration is repeated until the convergence of the overall system.

4.3.2.3 Results

Results show non-maxwellian behaviours in both plasma and neutral systems. The known phenomenology of discharge plasmas is retrieved: the plasma is neutral in the center (4 mm from the PG) while a charge region (the sheath) develops in contact to the grid. The importance of surface production is underlined comparing the two cases studied: plasma grid and extraction hole. In the first case the negative ion density increases by one order of magnitude respect to the case without surface production. In fig.36a is evident from the H^- profile the separate contribution from bulk and surface. It is also evident the effect of the magnetic filter in reducing the electron density near the plasma grid (the ratio $e:H^-$ is about 0.05). Finally, due to strong negative ion production on the surface and to the parallel magnetic filter, a complete reversed sheath is recovered (fig.36b) in agreement with different simulation results [155] and experimental measurements [156]. This abets the extractions of H^- from the source region towards the extraction grid.

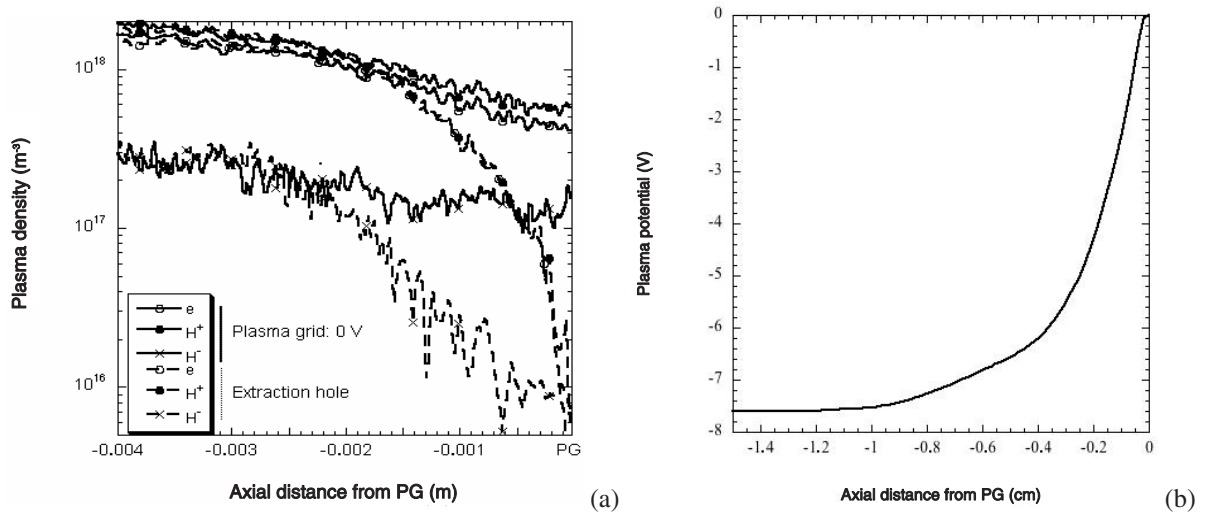


Fig. 36 Axial profile of (a) plasma density and (b) electric potential for the extraction region of the negative ion source as result of the simulation.

References

- [1] M. A. Lieberman, A. J. Lichtenberg, Principles of Plasma Discharges and Materials Processing (New York: Wiley, 1994).
- [2] Y. P. Raizer, M. N. Shneider, N. A. Yatsenko, Radio-Frequency Capacitive Discharges (Boca Raton, FL: CRC Press, 1995).

- [3] A. Bogaerts, E. Neyts, R. Gijbels, J. van der Mullen, *Spectrochimica Acta B* **57**, 609 (2002).
- [4] F. X. Bronold, K. Matyash, D. Tskhakaya, R. Schneider, H. Fehske, Radio-frequency discharges in Oxygen. I: Modeling, *J. Phys. D: Appl. Phys.* **40**, 6583 (2007).
- [5] K. Dittmann, D. Drozdov, B. Krames, J. Meichsner, Radio-frequency discharges in Oxygen. II: Spatio-temporally resolved optical emission pattern, *J. Phys. D: Appl. Phys.* **40**, 6593 (2007).
- [6] R. M. Hemsworth, J.-H. Feist, M. Hanada *et al.*, *Neutral beams for ITER*, *Rev. Sci. Instrum.*, **67**(3), 1120-1125 (1996).
- [7] M. Surendra, D. B. Graves, I. J. Morey, *Appl. Physics. Lett.* **56**, 1022 (1990).
- [8] D. Vender, R. W. Boswell, *J. Vac. Sci. Technol. A* **10**, 1331 (1992).
- [9] V. Vahedi, G. DiPeso, C. K. Birdall, M. A. Lieberman, T. D. Roglien, *Plasma Sources Sci. Technol.* **2**, 261 (1993).
- [10] V. Vahedi, C. K. Birdsall, M. A. Lieberman, G. DiPeso, T. D. Roglien, *Plasma Sources Sci. Technol.* **2**, 273 (1993).
- [11] M. M. Turner, R. A. Doyle, M. B. Hopkins, *Appl. Phys. Lett.* **62**, 3247 (1993).
- [12] M. Yan, A. Bogaerts, W. J. Goedheer, R. Gijbels, *Sci. Technol.* **9**, 583-591 (2000).
- [13] V. Ivanov, O. Proshina, T. Rakhimova, A. Rakhimov, D. Herrebout, A. Bogaerts, *J. Appl. Phys.* **91**, 6296 (2002).
- [14] A. L. Alexandrov, I. V. Schweigert, *Plasma Sources Sci. Technol.* **14**, 209-218 (2005).
- [15] V. Georgieva, A. Bogaerts, R. Gijbels, *J. Appl. Phys.* **94** (2003).
- [16] K. Matyash, R. Schneider, *Contrib. Plasma Phys.* **44**, 589 (2004).
- [17] N. Yu. Babaeva, J. K. Lee, J. W. Shon, *J. Phys. D: Appl. Phys.* **38**, 287-299 (2005).
- [18] V. Vahedi, M. Surendra, *Comput. Phys. Commun.* **87**, 179 (1995).
- [19] S. H. Lee, F. Iza, J. K. Lee, *Phys. Plasma* **13**, 057102 (2006).
- [20] V. A. Godyak, R. B. Piejak, *Phys. Rev. Lett.* **65**, 996 (1990).
- [21] E. Kawamura, M. A. Lieberman, A. J. Lichtenberg, *Phys. Plasmas* **13**, 053506 (2006).
- [22] I. D. Kaganovich, O. V. Polomarov, C. E. Theodosiou, *IEEE Trans. Plasma. Sci.* **34**, 696 (2004).
- [23] D. L. Tolliver, *VLSI Electronics: Microstructure Science*, ed. N. G. Einspruch, D. M. Brown (New York: Academic, 1984).
- [24] J. Siejka, J. Perriere, *Phys. Thin Films* **14**, 81 (1989).
- [25] D. A. Carl, D. W. Hess, M. A. Lieberman, T. D. Nguyen, R. Gronsky, *J. Appl. Phys.* **70**, 3301 (1991).
- [26] M. Kitajima, H. Kuroki, H. Shinno, K. G. Nakamura, *Solid State Comm.* **83**, 385 (1992).
- [27] M. Boutonnet-Kizling, S. G. Jaeras, *Appl. Catal. A* **147**, 1-21 (1996).
- [28] F. Nicolazo, A. Goullet, A. Granier, C. Vallee, G. Tubran, B. Grolleau, *Surf. Coat. Technol.* **98**, 1578 (1998).
- [29] J. Meichsner, M. Zeuner, B. Krames, M. Nitschke, R. Rochodzki, K. Barucki, *Surf. Coat. Technol.* **98**, 1565 (1998).
- [30] J. T. Gudmundsson, *J. Phys. D: Appl. Phys.* **37**, 2073 (2004).
- [31] J. T. Gudmundsson, A. M. Marakhtanov, K. K. Patel, V. P. Gopinath, M. A. Lieberman, *J. Phys. D: Appl. Phys.* **33**, 1323 (2000).
- [32] J. T. Gudmundsson, I. G. Kouznetsov, K. K. Patel, M. A. Lieberman, *J. Phys. D: Appl. Phys.* **34**, 1100 (2001).
- [33] J. Meichsner, M. Zeuner, B. Krames, M. Nitschke, R. Rochodzki, K. Barucki, *Surf. Coat. Technol.* **98**, 1565 (1998).
- [34] K. Matyash, Kinetic modeling of multi-component edge plasmas, Ph.D. thesis, University Greifswald, Germany (2003).
- [35] H. M. Katsch, T. Sturm, E. Quandt, H. F. Doebele, *Plasma Sources Sci. Technol.* **9**, 323 (2000).
- [36] C. Wild, P. Koidl, *Appl. Phys. Lett.* **54**, 505 (1989).
- [37] C. Wild, P. Koidl, *J. Appl. Phys.* **69**, 2909 (1991).
- [38] M. Fivaz, S. Brunner, W. Schwarzenbach, A. A. Howling, Ch. Hollenstein, *Plasma Sources Sci. Technol.* **4**, 373 (1995).
- [39] E. Kawamura, V. Vahedi, M. A. Lieberman, C. K. Birdsall, *Plasma Sources Sci. Technol.* **8**, R45 (1999).
- [40] J. Meichsner, private communication.
- [41] M. A. Lieberman, V. A. Godyak, *IEEE Trans. Plasma. Scie.* **26**, 955 (1998).
- [42] I. D. Kaganovich, V. I. Kolobov, L. D. Tsandin, *Appl. Phys. Lett.* **69**, 3818 (1996).
- [43] C. M. O. Mahony, J. McFarland, P. G. Steen, W. G. Graham, *Appl. Phys. Lett.* **75**, 331 (1999).
- [44] P. K. Shukla, A. A. Mamun, *Introduction to dusty plasma physics* (Institute of Physics Publishing, 2002).
- [45] S. V. Vladimirov, K. Ostrikov, *Physics Reports* **393**, 175-380 (2004).
- [46] G. S. Selwyn, J. Singh, R. S. Bennett, *J. Vac. Sci. Technol. A* **7**, 2758 (1989).
- [47] A. Bouchoule, *Dusty Plasmas: Physics, Chemistry and Technological Impacts in Plasma Processing* (John Wiley & Sons Ltd, 1999).
- [48] G. H. P. M. Swinkels, Optical studies of micron-sized particles immersed in a plasma, Ph.D. thesis, Eindhoven University of Technology, the Netherlands (1999).
- [49] R. J. Buss, S. V. Babu, *J. Vac. Sci. Technol. A* **14**, 577 (1996).
- [50] P. Roca i Cabarrocas, N. Layadi, M. Kunst, C. Clerc, H. Bernas, *J. Vac. Sci. Technol. A* **16**, 436 (1998).
- [51] D. M. Tanenbaum, A. L. Laracuate, A. Gallagher, *Appl. Phys. Lett.* **68**, 1705-1707 (1996).
- [52] J. Winter, G. Gebauer, *J. Nucl. Mater.* **266-269**, 228-233 (1999).
- [53] M. Rubel, M. Cecconello, J. A. Malmberg, G. Sergienko, W. Biel, J. R. Drake, A. Hedqvist, A. Huber, V. Philipps, *Nuclear Fusion* **41**, 1087 (2001).
- [54] J. Winter, V. E. Fortov, A. P. Nefedov, *J. Nucl. Mater.* **290-293**, 509 (2001).
- [55] J. Phillip Sharpe, *et al.*, *J. Nucl. Mater.* **313-316**, 455-459 (2003).

- [56] I. Narihara, et al., Nucl. Fusion **37**, 1177-1182 (1997).
- [57] A. Piel, A. Melzer, Plasma Phys. Control. Fusion **44**, R1 (2002).
- [58] C. Zafiu, A. Melzer, A. Piel, Phys. Plasmas **9**, 4794 (2002).
- [59] H. Ikezi, Phys. Fluids **29**, 1764 (1986).
- [60] J. H. Chu, Lin I, Physica A **205**, 183-190 (1994).
- [61] H. Thomas, G. E. Morfill, V. Demmel, J. Goree, B. Feuerbacher, D. Möhlmann, Phys. Rev. Lett. **73**, 652 (1994).
- [62] Y. Hayashi, K. Tachibana, Jpn. J. Appl. Phys. **33**, 804 (1994).
- [63] A. Melzer, T. Trottenberg, A. Piel, Phys. Lett. A **191**, 301-308 (1994).
- [64] J. B. Pieper, J. Goree, R.A. Quinn, Phys. Rev. **54**, 5636 (1996).
- [65] A. Melzer, A. Homann, A. Piel, Phys. Rev. E **53**, 2757 (1996).
- [66] G. E. Morfill, H. M. Thomas, U. Konopka, M. Zuzic, Phys. Plasmas **6**, 1769 (1999).
- [67] A. Homann, A. Melzer, S. Peters, R. Mandani, A. Piel, Phys. Lett. A **173**, 1 (1998).
- [68] A. Piel, V. Nosenko, J. Goree, Phys. Rev. Lett. **89**, 085004 (2002).
- [69] S. V. Vladimirov, Physica A **315**, 222 (2002).
- [70] D. Samsonov, J. Goree, Z. W. Ma, A. Bhattacharjee, H. M. Thomas, G. E. Morfill, Phys. Rev. Lett. **83**, 3649 (1999).
- [71] A. Melzer, S. Nunomura, D. Samsonov, Z. W. Ma, J. Goree, Phys. Rev. E **62**, 4162 (2000).
- [72] V. Vyas, G. A. Hebner, M. J. Kushner, J. Appl. Phys. **92**, 6451-6460 (2002).
- [73] M. R. Akdim, W. J. Goedheer, J. Appl. Phys. **94**, 104 (2003).
- [74] M. R. Akdim, W. J. Goedheer, Phys. Rev. E **67**, 056405 (2003).
- [75] G. Gozadinos, A.V. Ivlev, J. P. Boeuf, New Journal of Physics **5**, 32.1-32.9 (2003).
- [76] W. J. Goedheer, M. R. Akdim, Yu. I. Chutov, Contrib. Plasma Phys. **44**, 395 – 404 (2004).
- [77] J. E. Allen, Phys. Scripta **45**, 497-503 (1992).
- [78] I. H. Hutchinson, Plasma Phys. Control. Fusion **44**, 1953 (2002).
- [79] I. H. Hutchinson, Plasma Phys. Control. Fusion **45**, 1477 (2003).
- [80] I. H. Hutchinson, Plasma Phys. Control. Fusion **47**, 71 (2005).
- [81] I. H. Hutchinson, Plasma Phys. Control. Fusion **48**, 185 (2006).
- [82] R. Smirnov, Y. Tomita, D. Tskhakaya, T. Takizuka, Contrib. Plasma Phys. **46**, 623 (2006).
- [83] S. A. Maiorov, S. V. Vladimirov, N. F. Cramer, Phys. Rev. E **63**, 017401 (2001).
- [84] S. V. Vladimirov, S. A. Maiorov, N. F. Cramer, Phys. Rev. E **67**, 016407 (2003).
- [85] K. Matyash, R. Schneider, A. Bergmann, W. Jacob, U. Fantz, P. Pecher, J. Nucl. Matter. **313-316**, 434 (2003).
- [86] C. K. Birdsall, A. B. Langdon, Plasma physics via computer simulation (McGraw-Hill, New York, 1985).
- [87] S. Y. Vladimirov, M. Nambu, Phys. Rev. E **52**, R2172 (1995).
- [88] P. G. de Gennes, Superconductivity of Metals and Alloys (Benjamin, New York 1966).
- [89] F. Melandso, J. Goree, J. Vac. Sci. Technol. A **14**, 511 (1996).
- [90] V. A. Schweigert, I. V. Schweigert, A. Melzer, A. Homann, A. Piel, Phys. Rev. E **54**, 4155 (1996).
- [91] M. Lampe, G. Joyce, G. Ganguli, V. Gavrishchaka, Phys. Plasmas **7**, 3851 (2000).
- [92] M. Zuzic, A.V. Ivlev, J. Goree, G. E. Morfill, H. M. Thomas, H. Rothermel, U. Konopka, R. Sütterlin, D. D. Goldbeck, Phys. Rev. Lett. **85**, 4064 (2000).
- [93] G. E. Morfill, B. M. Annaratone, P. Bryant, A. V. Ivlev, H. M. Thomas, M. Zuzic, V. E. Fortov, Plasma Phys. Control. Fusion **44**, B263 (2002).
- [94] K. Matyash, R. Schneider, Contributions to Plasma Physics **44**, 157 (2004).
- [95] K. Matyash, M. Fröhlich, H. Kersten, G. Thieme, R. Schneider, M. Hannemann, R. Hippler, J. Phys. D: Appl. Phys. **37**, 2703 (2004).
- [96] O. Arp, D. Block, M. Klindworth, A. Piel, Phys. Plasmas **12**, 122102 (2005).
- [97] M. Bacal, A. Hatayama, J. Peters, IEEE Trans. on Plasma Sci. **33**, 1845 (1996).
- [98] Combined ITER NBI R&D Review and JA-EU Workshop, Naka, Japan, (December 13-17, 2006).
- [99] J. N. M. van Wunnik, J. J. C. Geerlings, E. H. A. Granneman, J. Los, Surf. Sci. **131**, 17 (1983).
- [100] K. Shinto, et al Japan J. Appl. Phys. **35**, 1894 (1996).
- [101] M. Hanada, T. Seki, N. Takado, T. Inoue, A. Hatayama, M. Kashiwagi, K. Sakamoto, M. Taniguchi, K. Watanabe, Nucl. Fusion **46**, S318-S323 (2006).
- [102] M. Hanada, T. Seki, N. Takado, T. Inoue, H. Tobari, T. Mizuno, A. Hatayama, M. Dairaku, M. Kashiwagi, K. Sakamoto, M. Taniguchi, K. Watanabe, Rev. Sci. Instrum. **77**, 03A515 (2006).
- [103] N. Takado, J. Hanatani, T. Mizuno, K. Katoh, A. Hatayama, M. Hanada, T. Seki, T. Inoue, Rev. Sci. Instrum. **77**, 03A533 (2006).
- [104] N. Takado, J. Hanatani, T. Mizuno, K. Katoh, A. Hatayama, H. Tobari, M. Hanada, T. Inoue, M. Taniguchi, M. Dairaku, M. Kashiwagi, K. Watanabe, K. Sakamoto, "Numerical analysis of the hydrogen atom density in a negative ion source", in Proceedings of the 11th Int. Symposium on the Production and Neutralization of Negative Ions and Beams (Santa-Fe, USA, September 2006).
- [105] N. Takado, H. Tobari, T. Inoue, J. Hanatani, A. Hatayama, M. Hanada, M. Kashiwagi, K. Sakamoto, submitted to J. Appl. Phys.
- [106] B. Rasser, J. N. M. Van Wunnik, J. Los, Surf. Sci. **118**, 697 (1982).

- [107] M. Seidl, H. L. Cui, J. D. Isenberg, H. J. Kwon, B. S. Lee, T. Melnychuk, J. Appl. Phys. **79**, 2896 (1996).
- [108] H. Tobari, T. Seki, N. Takado, M. Hanada, T. Inoue, M. Kashiwagi, A. Hatayama, K. Sakamoto, Plasma and Fusion Res. **2**, 022 (2007).
- [109] D. Riz, J. Paméla, "Modeling of Negative Ion Transport in a Plasma Source", AIP Conf. Proceedings No 439 (Villagium of Giens, France 1997) 62-73.
- [110] D. Riz, J. Pamela, Rev.Sci. Instrum. **69**, 914-919 (1998).
- [111] Y. Uematsu, T. Morishita, A. Hatayama, T. Sakurabayashi, M. Ogasawara, Rev. Sci. Instrum. **71**, 883-886 (2000).
- [112] A. Hatayama, T. Sakurabayashi, Y. Ishi, K. Makino, M. Ogasawara, M. Bacal, Rev. Sci. Instrum. **73**, 910-913 (2002).
- [113] K. Makino, T. Sakurabayashi, A. Hatayama, K. Miyamoto, M. Ogasawara, Rev. Sci. Instrum. **73**, 1051-1053 (2002).
- [114] O. Fukumasa, T. Fujita, T. Fukuchi, Modeling of Negative Ion Transport in Hydrogen Ion Sources - Estimation of Extracted H^- Current, AIP Conf. Proceedings No 639 (Gif-sur-Yvette, France 2002) 75-81.
- [115] A. Hatayama, K. Makino, T. Sakurabayashi, K. Miyamoto, M. Ogasawara, M. Bacal, Rev. Sci. Instrum. **75**, 1650-1653 (2004).
- [116] Y. Matsumoto, M. Nishiura, K. Matsuoka, M. Sasao, M. Wada, H. Yamaoka, Thin. Solid. Films **506-507**, 522 (2006).
- [117] O. Fukumasa, R. Nishida, Nucl. Fusion **46**, S275 (2006).
- [118] F. El Balghiti-Sube, F. G. Baksht, M. Bacal, Rev. Sci. Instrum. **67**, 2221 (1996).
- [119] T. Sakurabayashi, A. Hatayama, M. Bacal, J. Appl. Phys. **95**, 3937 (2004).
- [120] T. Sakurabayashi, A. Hatayama, M. Bacal, Effects of Transverse Magnetic Field and Spatial Potential on Negative transport in Negative ion sources, in Proceedings of the 10th International Symposium on the Production and Neutralization of Negative Hydrogen Ions and Beams (Kiev, Ukraine, 2004) 75-81.
- [121] A. Hatayama, T. Matsumiya, T. Sakurabayashi, M. Bacal, Rev. Sci. Instrum. **77**, 03A530 (2006).
- [122] A. Hatayama, Progress in Modeling and Numerical Simulation of Negative Hydrogen Ion Sources, to be published in Rev. Sci. Instrum.
- [123] Y. Ohara, M. Akiba, H. Horiike, H. Imai, Y. Okumura, S. Tanaka, J. Appl. Phys. **61**, 1323 (1987).
- [124] E. Speth, H. D. Falter, P. Franzen et al., Nucl. Fus. **46**, S220-S238 (2006).
- [125] M. Bacal, *Physics aspects of negative ion sources*, Nucl. Fus. **46**, S250-S259 (2006).
- [126] F. Taccogna, R. Schneider, S. Longo, M. Capitelli, Phys. Plasmas **14**, 073503 (2007).
- [127] M. Bandyopadhyay, Studies of an inductively coupled negative hydrogen ion radio frequency source through simulations and experiments, PhD thesis, (Technische Universitat Munchen, Max-Planck-Institut fur Plasmaphysik, Garching, Germany, 2004).
- [128] U. Fantz, H. D. Falter, P. Franzen, E. Speth, R. Hemsworth, D. Boilson, A. Krylov, Rev. Sci. Instrum. **77**, 03A516 (2006).
- [129] U. Fantz, H. Falter, P. Franzen, D. Wunderlich, M. Berger, A. Lorenz, W. Kraus, P. McNeely, R. Riedl, E. Speth, Nucl. Fus. **46**, S297-S306 (2006).
- [130] M. Furudate, K. Fujita, T. Abe, J. Thermophys. Heat Transf. **20**, 457-464 (2006).
- [131] R. Celiberto, R. K. Janev, A. Laricchiuta, M. Capitelli, J. M. Wadehra, D. E. Atems, At. Data and Nucl. Data Tables, **77**, 161-213 (2001).
- [132] R. Celiberto, M. Capitelli, A. Laricchiuta, Physica Scripta **T96**, 32-44 (2002).
- [133] P. S. Krstić, D. R. Schultz, Elastic and vibrationally inelastic slow collisions: $H+H_2$, H^++H_2 , J. Phys. B: At. Mol. Opt. Phys. **32**, 2415-2431 (1999); see also <http://www-cfadc.phy.ornl.gov>.
- [134] P. S. Krstić, D. R. Schultz, Elastic processes involving vibrationally excited molecules in cold hydrogen plasmas, J. Phys. B: At. Mol. Opt. Phys. **36**, 385-398 (2003); see also <http://www-cfadc.phy.ornl.gov>.
- [135] P. S. Krstić, D. R. Schultz, R. K. Janev, Charge transfer processes in slow collisions of protons with vibrationally excited hydrogen molecules, Phys. Scripta **T96**, 61-71 (2002); see also <http://www-cfadc.phy.ornl.gov>.
- [136] P. S. Krstić, Inelastic processes from vibrationally excited states in slow H^++H_2 and $H+H_2^+$ collisions: excitations and charge transfer, Phys. Rev. **A66**, 042717 (2002); see also <http://www-cfadc.phy.ornl.gov>.
- [137] P. S. Krstić, R. K. Janev, Inelastic processes from vibrationally excited states in slow H^++H_2 and $H+H_2^+$ collisions. II. Dissociation, Phys. Rev. **A67**, 022708 (2003); see also <http://www-cfadc.phy.ornl.gov>.
- [138] R. K. Janev, W. D. Longer, K. Evants, Jr., D. E. Post, Elementary Processes in Hydrogen-Helium Plasmas (Springer, Berlin, 1987).
- [139] F. Esposito, M. Capitelli, Atomic and Plasma-Material Interaction Data for Fusion, **9**, 65-73 (2001).
- [140] P. Minelli, D. Bruno, S. Longo, M. Capitelli, private communication, (2007).
- [141] K. Nanbu, IEEE Trans. Plasma Sci. **28**, 971 (2000).
- [142] A. Fridman, L. A. Kennedy, Plasma Physics and Engineering (Taylor & Francis, New York, 2004).
- [143] M. Capitelli, C. M. Ferreira, B. F. Gordiets, A. I. Osipov, Plasma kinetics in atmospheric gases, (Springer, Berlin, 2000).
- [144] D. Shalashilin, B. Jackson, M. Persson, J. Chem. Phys. **110**, 11038-11046 (1999).
- [145] G. D. Billing, M. Cacciatore, Recombination coefficient and final state vibrational distribution for the reaction: $H+H_a+Cu(111) \rightarrow H_2(v)+Cu(111)$, Proceedings of the 7th International Symposium on Production and Neutralization of Negative Ions and Beams, edited by K. Prelec (AIP Conf. Proc. No. 380 American Institute of Physics, New York, 1995) 118.

- [146] B. Jackson, D. Lemoine, J. Chem. Phys. **114**, 474-482 (2001).
- [147] W. Eckstein, J. P. Biersack, Appl. Phys. **A38**, 123-129 (1985).
- [148] E. Molinari, M. Tomellini, Chem. Phys. **270**, 439-458 (2001).
- [149] R. I. Hall, I. Čadež, M. Landau, F. Pichou, C. Schermann, Phys. Rev. Lett. **60**, 337-340 (1988).
- [150] P. J. Eenshuistra, J. H. M. Bonnie, J. Los, H. J. Hopman, Phys. Rev. Lett. **60**, 341-344 (1988).
- [151] J. R. Hiskes, A. M. Karo, J. Appl. Phys. **67**, 6621 (1990).
- [152] I. Méndez, F. J. Gordillo-Vázquez, V. J. Herrero, I. Tanarro, J. Phys. Chem. **A110**, 6060-6066 (2006).
- [153] O. Fukumasa, M. Hosoda, H. Naitou, Rev. Sci. Instrum. **63**, 2696-2698 (1992).
- [154] H. Takahashi, T. Kasuya, M. Wada, Rev. Sci. Instrum. **77**, 03A513 (2006).
- [155] R. Becker, Rev. Sci. Instrum. **77**, 03A504 (2006).
- [156] M. Bandyopadhyay, A. Tanga, H. D. Falter, P. Franzen, B. Heinmann, D. Holtum, W. Kraus, K. Lackner, P. McNeely, R. Riedl, E. Speth, R. Wilhelm, J. Appl. Phys. **96**, 4107-4113 (2004).
- [157] J. R. Hiskes, A. Karo, M. Gardner, J. Appl. Phys. **47**, 3888-3896 (1976).
- [158] Yu. Belchenko, Rev. Sci. Instrum. **64**, 1385-1393 (1993).